공학박사 학위논문

A-site modification effect of 2-dimensional dielectric nanosheets

A-site 치환에 따른 2차원 유전체 나노시트의 특성 분석

2018 년 8 월

서울대학교 대학원

화학생물공학부

임 해 나

Abstract

A-site modification effect of 2-dimensional dielectric nanosheets

Haena Yim

School of Chemical and Biological Engineering

The Graduate School

Seoul National University

The demand for high-k dielectric thin films have been continuously increasing to satisfy the requirement of next-generation electronic devices such as ultra-thin dielectric layer in high capacitance multilayer ceramic capacitors and gate dielectric for high mobility thin film transistor. In addition, as these devices are becoming highly integtraed, the thickness of dielectric layer should be reduced under tens of nanometers. The well-known dielectric films for capacitors are $BaTiO_3$ based perovskites. However, these materials usually decrease their dielectric permittivity as thickness reduces because of the size-effect; the dielectric properties are dependent on the grain size of materials due to its decreased particle size and show different behavior from a single crystal.

One of the new methodologies to solve current problems is using two-dimensional (2D) nanosheets thin films. Especially, Dion-Jacobson phases nanosheets have received attention. For example, $Ca_2Nb_3O_{10}$ (ε_r = 200) and $Sr_2Nb_3O_{10}$ (ε_r = 240) nanosheets show high-k dielectric permittivity undisturbed for thickness and low dielectric loss at the same time. These nanosheets can easily be synthesized by exfoliation of layered perovskite compound $K(Ca \text{ or } Sr)_2Nb_3O_{10}$ as a parent materials.

The intercalated K^+ ions between (Ca or Sr)$_2Nb_3O_{10}$ perovskite slabs are sequentially exchanged by H^+ ions and TBA^+ ions. When the large organic TBA^+ ions are intercalated to the perovskite slabs, each negatively charged perovskite layers are naturally delaminated due to the swelling. Consequently, we can easily obtain single crystal (Ca or Sr)$_2Nb_3O_{10}$ perovskite nanosheets. Moreover, 2D nanosheets thin films do not require post annealing process due to their crystalline nature, so it facilitates deposition on various substrates including polymer. Also, we can easily control the composition of nanosheets by modification of parent material.

However, the dielectric constant is still far below the bulk value and the question for electrical properties of single nanosheet still remains. Therefore, we worked on exploring new composition Dion-Jacobson phases based on niobate by A-site mofidication and investigating the properties of single nanosheet. In this thesis, we focused on $Sr_2Nb_3O_{10}$ based perovskite nanosheets. We have confirmed the behavior of dielectric and structural properties in $KSr_{2(1-x)}M_{2x}Nb_3O_{10}$ (M = Ca, Bi, Ag) bulk ceramics as well as in nanosheets form. The nanosheets thin film deposition process was performed by the electrophoretic deposition method (EPD) and the Langgmuir-Blodgett (LB) deposition method.

After a brief background with the previous research work on 2D dielectric nanosheets thin films in chapter 1, the structural and dielectric properties of layered perovskite $KCa_{2(1-x)}Sr_{2x}Nb_3O_{10}$ and $HCa_{2(1-x)}Sr_{2x}Nb_3O_{10}$ ceramic, which incorporates starting materials for $Ca_2Nb_3O_{10}$ and $Sr_2Nb_3O_{10}$ dielectric nanosheet compositions, are investigated in chapter 2. The dielectric permittivity is gradually increased with increasing Sr substitution due to the large ionic polarizability of Sr^{2+} ions in the lattice. Also, we synthesized $Ca_2Nb_3O_{10}$ and $Ca_{0.8}Sr_{1.2}Nb_3O_{10}$ nanosheets and deposited to thin films by EPD. Similar to bulk materials, the dielectric permittivity of thin films was enhanced with increasing Sr content in the lattice.

In the next two chapters, we demonstrate the A-site engineering of dielectric

materials in the formula of $KSr_{2(1-x)}M_{2x}Nb_3O_{10}$. In chapter 3, we discuss the improvement in dielectric properties when the A-site located Sr ions are substituted by the higher polarizable Bi ions. The dielectric permittivity of $KSr_{2(1-x)}Bi_{2x}Nb_3O_{10}$ gradually increases from 31 to 348 while the dielectric loss decreases from 0.111 to 0.040 at 1 MHz as a consequence of substituting Bi cations for Sr cations. Enhanced dielectric properties are examined by RAMAN and DFT calculations. Also, $Sr_{2(1-x)}Bi_{2x}Nb_3O_{10}$ (x = 0, 0.1, 0.2, 0.3) colloidal nanosheets were successfully synthesized through 2-step cation exchanging process. In chapter 4, A-site located Sr ions are substituted by higher polarizable Ag ions. The dielectric properties are enhanced with the increase of Ag content in bulk ceramic, but there is secondary phase with aggromated Ag metal after x = 0.1. Therefore, we only synthesized dielectric nanosheets with x = 0.1 composition. $HSr_{1.8}Ag_{0.2}Nb_3O_{10}$ ceramic, which is the medium materials for exfoliation, is well obtained and showed enhanced dielectric permittivity from 96.6 to 332 with dielectric loss from 0.4 to 0.03 by Ag substitution. Moreover, the $Sr_{1.8}Ag_{0.2}Nb_3O_{10}$ colloidal nanosheets were successfully synthesized.

Among the synthesized perovskite nanosheets, the Bi-substituted $Sr_2Nb_3O_{10}$ nanosheets show the most stable and excellent fabrication yield. Therefore, in chapter 5, we investigate the properties of multilayer thin films with $Sr_{1.8}Bi_{0.2}Nb_3O_{10}$ nanosheets. The 10 layer stacked thin film was deposited by Langmuir-Blodgett method and has shown twice higher dielectric permittivity than $Sr_2Nb_3O_{10}$. Moreover, we deposit thin films on transparent and flexible substrate to demonstrate the possibility of developing transparent and flexible dielectric capacitors.

Keywords: Landmuir-Blodgett deposition, dielectric nanosheets, dielectric capacitors, A-site modification, strontium niobate

Contents

List of Tables

Chapter 1

Chapter 5

List of Figures

Chapter 1

Chapter 2

Chapter 3

Chapter 4

Chapter 5

Chapter 1. Introduction

1.1. General introduction to dielectric

A dielectric material is an insulator that exhibit electric polarization under applied electric field. Dielectric materials have been required for various electronic devices such as multilayer ceramic capacitors (MLCCs), sensors, memories, and gate insulators[1]. The direction of improvement in these devices generally has been going toward the miniaturization with gaining a higher dielectric constant and lower dielectric loss, but there is a limitation for downsizing. For example, the capacitance of MLCCs, which are composed with the many alternated dielectric and electrode layers, is determined by number of layers, dielectric constant, active area, and the thickness of dielectric layers as following formula:

C (the capacitance of the MLCCs) = $[\varepsilon_r \cdot \varepsilon_0 \cdot (n-1) \cdot s] / t$

where ε_r = the relative permittivity of the dielectric films; ε_0 = the permittivity of the free space; n = the number of dielectric layers; s = the overlapping area of the internal electrode; t = the thickness of the dielectric layers.

Therefore, the thickness of dielectric layer should be reduced as much as possible in order to increase capacitance, so the enormous researches on downsizing of dielectric layer has been actively studied. However, synthetic spherical nano-sized powder for dielectric thin film is difficult and involves much expense. Besides, the conventional dielectric materials such as $PbTiO_3$ and $BaTiO_3$-based perovskites show the degradation of dielectric responses as decreasing thickness, which called as size-effect[2]. For example, the dielectric permittivity of $BaTiO_3$ ceramics powder are strongly affected by particle sizes and more sensitively reduced below 250 nm grain size. The thickness dependence dielectric permittivity is shown in Fig. 1[3-7].

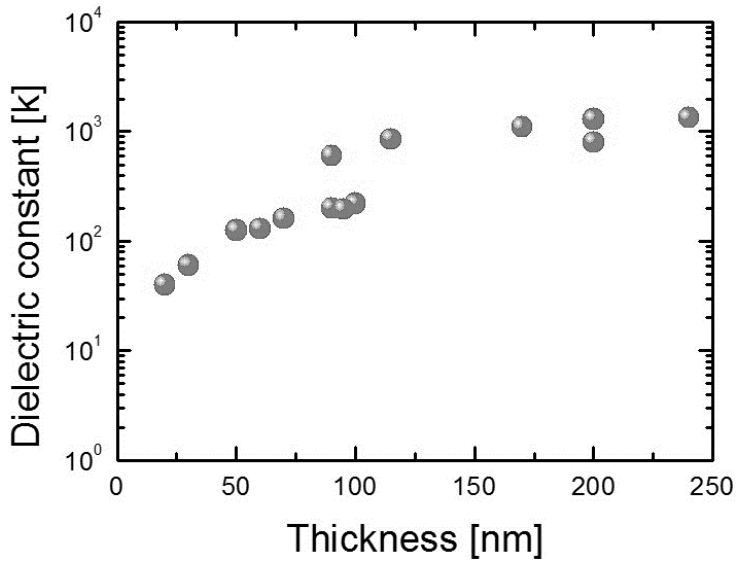

Figure 1.1. Dielectric permittivity of $BaTiO_2$ thin films according to thickness[3-7].

The origin of size-effect in dielectric has not been proven, but there are two models to explain an interfacial low-k dead layer[8], one of which is intrinsic model and the other is the extrinsic model. The intrinsic effect is cause by uncompensated dipoles, which generate depolarization field that reverses to the applied electric field, between dielectric and metal electrode layer. As a result, the opposite depolarization field reduces the dielectric permittivity and adversely affects to dielectric films. Therefore, this intricsic effect can be reduced by selecting an appropriate substrate. For example, thin film capacitors with atomistically smooth interfaces shows the better dielectric properties as decreaseing dead layer at the metal-dielectric interface[9]. The extrinsic effect is caused by the various defects occused during the high-temperature annealing process. Therefore, various technique such as controlling oxygen parial pressures during the annleaing[10], using self-standing perovskite[11], and controlling the fine grain size[12] are performed to minimize defects associated. However, it is still difficult to remove the size-effect in thin films fabricated from spherical particles. Thus, searching new direction of thin film fabrication with new type dielectric materials is urgently required for advanced devices.

1.2. 2-dimensional dielectric nanosheets

2-dimensional (2D) dielectric nanosheets have been considered as an excellent candidates for future electronic applications because of its unique structures and properties[13]. Pioneering studies about the dielectric naosheets was started in the 1990s by Sasaki et al., who reported the single titanate nanosheets, which produced by cation intercalation process in liquid from layered titanates ceramics[14]. The single crystal Titania nanosheets have attracted attention because of its higher dielectric constant than other deposited thin films. Titania nanosheet thin films possess Ti vacancies without oxygen vacancie, while other deposited Titania films often have problem of oxygen vacancies acting carrier traps and high-leakage paths.

Likewise, various oxide nanosheets such as single layers Mn oxides and several perovskites have been fabricated by 2-step cation exchange process (Fig. 1.2). The most-established method of exfoliation is intercalation with bulky guest ions such as tetrabutylammonium (TBA) and tetrametylammonium (TMA) ions. Before intercalation of bulky ions, the cation between the layered compounds are exchanged with proton ions, which the interlayer alkali metal ions can be completely removed while remaining the layered structure[15-17]. Table 1.1 shows the summary of reported nanosehets with ther parent layered perovskites.

Among the various 2D dielectric nanosheets, the layered perovskites have been attracted attention due to its great chemical activity including photocatalytic activity, ferroelectricity, dielectric and piezoelectricity[18]. Especially, Dion-Jacobson (DJ) phases layered perovskite materials such as $LaNb_2O_7$, $KCa_2Nb_3O_{10}$, and $KSr_2Nb_3O_{10}$ have been widely investigated. DJ phases have the formula $A'[A_{n-1}B_nO_{3n+1}]$ where A' is an intercalated alkali metal and $A_{n-1}B_nO_{3n+1}$ perovskite slabs. In case of DJ phase $KCa_2Nb_3O_{10}$, K^+ ions are intercalated $Ca_2Nb_3O_{10}^-$ perovskite slabs composed of corner-sharing NbO_6 octahedra and Ca ions[19,20].

These layered niobate are actively discussed and studied due to its changeable properties from an electrical insulator to a metal by doping of niobate layer. It is well-known that the properteis of perovskite materials are greatly influenced by A-site and B-site modification. The A-site substitution is known to improve dielectric properties, and B-site substitution is known to exhibit excellent leakage or fatigue properties by reducing oxygen deficiency. Also, these layered materials consist of negatively charged perovskite slabs and occupied cations in the interlayer space, so these materials have weak bonding between each perovskite layers (Fig. 1.3).

Therefore, the intercalated cation can be easily changed so that a various single crystal nanosheet can be simply delaminated into their elemental layers by exfoliating the layered structure precursors. Recently, Osada et al. reported Dion-Jacobson phase dielectric nanosheets thin films (Fig. 1.4). They delaminated nanosheets from layered perovskites ceramics and deposite thin films by Langmuir-Blodgett method on atomically flat Nb-doped $SrTiO_3$, $SrRuO_3$, and Pt substrates[7]. The thickness of thin films are between 5 and 20 nm. Among the three layer slab perovskite nanosheets, the $Sr_2Nb_3O_{10}$ films showed highest dielectric constants above 240 with low leakage current densities of below 10^{-7} A cm^{-2}.

Parent compound	Nanosheets	Dielectric permittivity	Refs.
$KCa_2Nb_3O_{10}$	$Ca_2Nb_3O_{10}$	200	21
$KSr_2Nb_3O_{10}$	$Sr_2Nb_3O_{10}$	240	22
$KLaNb_2O_7$	$LaNb_2O_7$	45	23
$CsBiNb_2O_7$	$BiNb_2O_7$	-	24
$KCaLaNb_2TiO_{10}$	$CaLaNb_2TiO_{10}$	-	25

Table 1.1. Type of Dion-Jacobcon nanosheets and their parent layered coumpound.

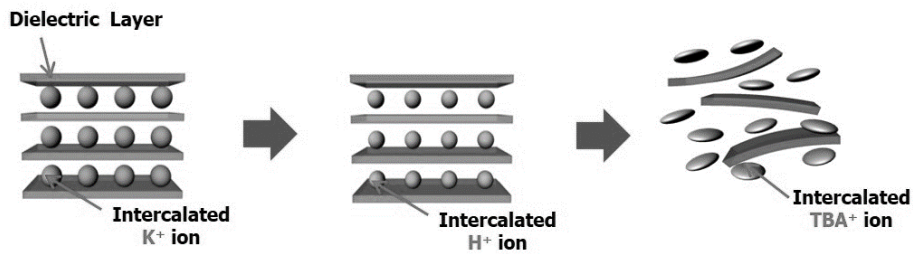

Figure 1.2. 2-step cation exchange process for exfoliation layered compound.

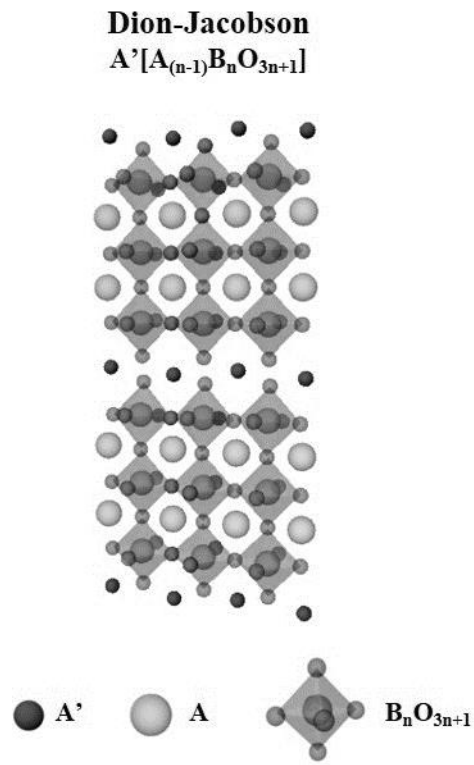

Figure 1.3. Structure of the Dion-Jacobson phase A'$[A_{(n-1)}B_nX_{(3n+1)}]$.

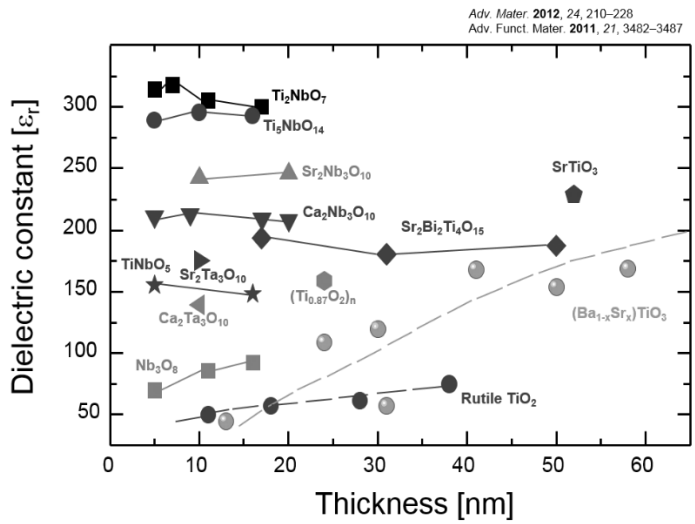

Figure 1.4. Dielectric permittivity of various dielectric nanosheets.

1.3. Langmuir-Blodgett method

These simply obtained single crystal nanosheet can be assembled as thin films on a various substrate by room temperature deposition processes such as Langmuir-Blodgett method, Layer-by-Layer process, and electrophoretic deposition. As a result, the post annealing process is not required which causes thermal damage on dielectric thin film, so the dielectric properties are invariant depending on the thickness. Because of this fabulous characteristic, using two dimensional dielectric nanosheet have received enormous attention as a new direction to fabricate nano-scaled dielectric thin film.

Among various deposition technique, Langmuir-Blodgett method is the best for the controlling thickness.It provides the high quality monolayer thin film and the precise control of the number of layers. In the Langmuir-Blodgett process, an insoluble nanoparticles or nanosheets are spread on the surface of solution such as DI water in the bath (Fig. 1.5 (a)). Then, the barriers compress particles to be monolayer. At the same time, the surface pressure changes are monitored by platinum plate with a force sensor, so that we can choose the appropriate density of monolayer. The monitored surface pressure is presented as the surface pressure-molecular area (π-A) isotherm curve where surface pressure (π) is measured as a function of molecular area (A).

As shown in Fig. 1.5 (b), a typical isotherm can be described as follows: at the beginning of the compression, monolayers are in a two-dimensional gaseous (G) phase. As increasing the compression, the monolayer is changed to a liquid-expanded (LE) phase. Further compression results in transition of the LE phase to the liquid-condensed (LC) phase, finally leading to a close packed solid (S) phase. Therfore, we can choose the appropriate phase according to the isotherm graph[26].

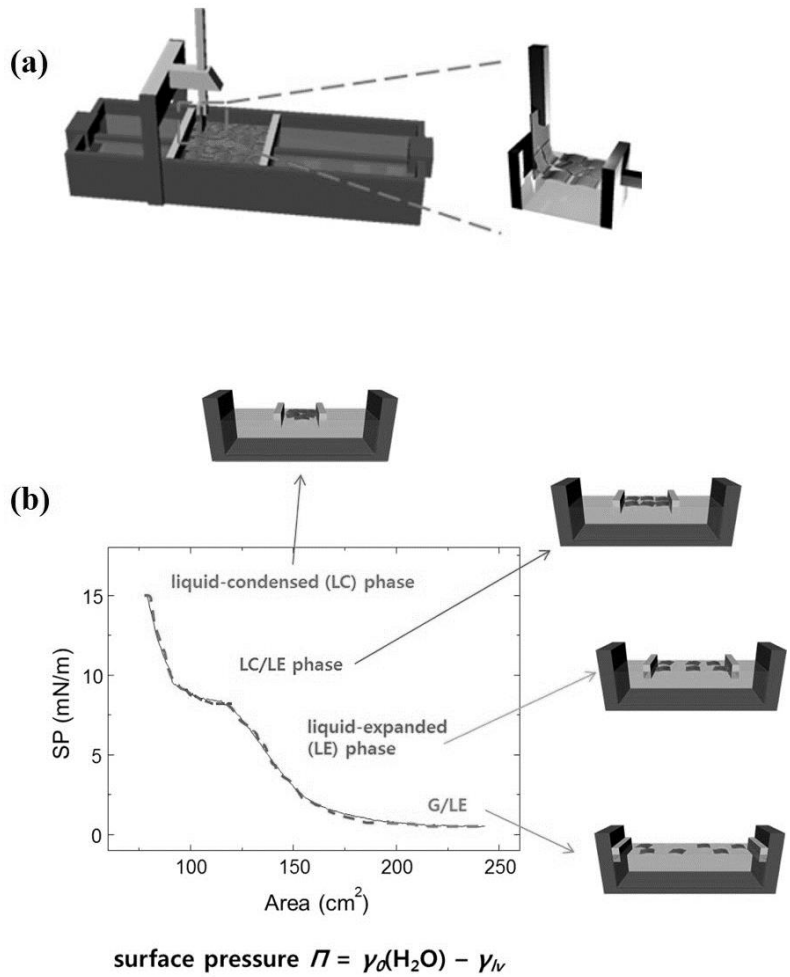

Figure 1.5. (a) Schemetic diagram of Langmuir-blodgett (b) the isotherm graph according to the surface presser

1.4. Main work of this thesis

In this thesis, we address the A-site modification effects in Dion-jacobson phase dielectric materials and fabrication of nanosheets thin films. For this study, we suggest important subjects to be studied.

(1) Synthesis and characterization of Sr-substituted $KCa_2Nb_3O_{10}$ dielectric materials according to the Sr substitution amount

(2) Synthesis and characterization of (Bi or Ag)-substituted $KSr_2Nb_3O_{10}$ dielectric materials to enhance their dielectric properteis

(3) Exfoliation of $KSr_{1.8}Bi_{0.2}Nb_3O_{10}$ and $KSr_{1.8}Ag_{0.2}Nb_3O_{10}$ to obtain single crystal dielectric nanosheets

(4) Assembly of nanosheets thin film for dead-layer-free dielectric by Langmuir-Blogdett method in room temperature

(5) Characterization of dielectic nanosheets thin films

Dion-Jacobson layered perovskites $KCa_{2(1-x)}Sr_{2x}Nb_3O_{10}$ were synthesized by solid-state reaction, and proton ions were exchanged to produce $HCa_{2(1-x)}Sr_{2x}Nb_3O_{10}$. We measured the structural and dielecric properties according to the Sr substitution amount in order to understanding A-site modification effect. Then, nanosheets were obtained by exfoliation of $HCa_{2(1-x)}Sr_{2x}Nb_3O_{10}$ and deposited to thin films by electrophoretic deposition method (chapter 2).

Next, Dion-Jacobson layered perovskite $KSr_{2(1-x)}M_{2x}Nb_3O_{10}$ (M = Bi, Ag) were synthesized by solid-state reaction (chapter 3 and chapter 4, respectively). The structural and dielecric properties of both bulk ceramics were investigated and $Sr_{1.8}M_{0.2}Nb_3O_{10}$ (M = Bi, Ag) nanosheets were obtained.

In chapter 5, we investigate the structural and dielectric charactization of $Sr_{1.8}Bi_{0.2}Nb_3O_{10}$ thin films which deposited by Langmuir-Blodgett deposition method. Moreover, we realized transparent flexible dielectric capacitor as deposition $Sr_{1.8}Bi_{0.2}Nb_3O_{10}$ thin films on oxide/metal/oxide transparent conducting oxide as

follow: top electrode (Zn-doped SnO_2 oxide/metal/ Zn-doped SnO_2 oxide)/ 10 layer of $Sr_{1.8}Bi_{0.2}Nb_3O_{10}$ / bottom electrode (Zn-doped SnO_2 oxide/metal/ Zn-doped SnO_2 oxide).

1.5. References

[1] B. C. Luo, X. H. Wang, E. K. Tian, H. Z. Song, Q. C. Zhao, Z. M. Cai, W. Feng and L. T. Li, J Eur Ceram Soc, 38, 1562 (2018).

[2] Z. J. Xu, R. Q. Chu, J. G. Hao, Y. J. Zhang, G. R. Li and Q. R. Yin, Physica B, 404, 2045 (2009).

[3] S. S. N. Bharadwaja, A. Rajashekhar, S. W. Ko, W. Qu, M. Motyka, N. Podraza, T. Clark, C. A. Randall and S. Trolier-McKinstry, J Appl Phys, 119 (2016).

[4] T. Pecnik, S. Glinsek, B. Kmet and B. Malic, J Alloy Compd, 646, 766 (2015).

[5] X. Ning, S. M. Chen, J. Y. Zhang, H. Huang and L. Wang, Appl Phys Lett, 107 (2015).

[6] N. Y. Chan, D. Y. Wang, Y. Wang, J. Y. Dai and H. L. W. Chan, J Appl Phys, 115 (2014).

[7] M. Osada and T. Sasaki, Adv Mater, 24, 210 (2012).

[8] M. Stengel and N. A. Spaldin, Nature, 443, 679 (2006).

[9] M. S. Majdoub, R. Maranganti and P. Sharma, Phys Rev B, 79 (2009).

[10] J. F. Ihlefeld, A. M. Vodnick, S. P. Baker, W. J. Borland and J. P. Maria, J Appl Phys, 103 (2008).

[11] L. W. Chang, M. McMillen, F. D. Morrison, J. F. Scott and J. M. Gregg, Appl Phys Lett, 93 (2008).

[12] C. A. Randall, N. Kim, J. P. Kucera, W. W. Cao and T. R. Shrout, J Am Ceram Soc, 81, 677 (1998).

[13] M. Osada and T. Sasaki, J Mater Chem, 19, 2503 (2009).

[14] T. Sasaki, M. Watanabe, H. Hashizume, H. Yamada and H. Nakazawa, J Am Chem Soc, 118, 8329 (1996).

[15] T. Sasaki and M. Watanabe, J Am Chem Soc, 120, 4682 (1998).

[16] M. M. J. Treacy, S. B. Rice, A. J. Jacobson and J. T. Lewandowski, Chem. Mater., 2, 279 (1190).

[17] R. E. Schaak and T. E. Mallouk, Chem. Mater., 14, 1455 (2002).

[18] J. H. Choy, J. Y. Kim, S. J. Kim, J. S. Sohn and O. H. Han, Chem Mater, 13, 906 (2001).

[19] H. Fukuoka, T. Isami and S. Yamanaka, J Solid State Chem, 151, 40 (2000).

[20] L. Viciu, N. Liziard, V. Golub, T. A. Kodenkandath and J. B. Wiley, Mater Res Bull, 39, 2147 (2004).

[21] B. W. Li, M. Osada, Y. Ebina, K. Akatsuka, K. Fukuda and T. Sasaki, Acs Nano, 8, 5449 (2014).

[22] B. W. Li, M. Osada, K. Akatsuka, Y. Ebina, T. C. Ozawa and T. Sasaki, Jpn J Appl Phys, 50 (2011).

[23] M. Osada and T. Sasaki, Low-Dimensional Nanoscale Electronic and Photonic Devices 5 -and- State-of-the-Art Program on Compound Semiconductors 54 (Sotapocs 54), 50, 111 (2012).

[24] T. Sivakumar and J. Gopalakrishnan, Mater Res Bull, 40, 39 (2005).

[25] J. Gopalakrishnan, S. Uma and V. Bhat, Chem Mater, 5, 132 (1993).

[26] K. Ariga, Y. Yamauchi, T. Mori, and J. P. Hill, Adv Mater, 25, 6477 (2013).

Chapter 2. Fabrication and characterization of Sr-substituted $KCa_2Nb_3O_{10}$ ceramics

2.1. Introduction

In chapter 1, we have descripted the infortance of the developing new Dion-Jacosbon phase perovskite nanosheets and understanding properties of mother materials for nanosheets. In this chapter, we focuses on the substitution of Sr^{2+} ions by Ca^{2+} ions in $KCa_2Nb_3O_{10}$ ceramics, which is mother materials of $Ca_2Nb_3O_{10}$ and $Sr_2Nb_3O_{10}$ nanosheets, in order to study its dieletric response according to the A-site ions.

The layered perovskite oxides are especially considered to have enormous potential because of their property variability from changing ions between the perovskite layers through simple chemical ion-exchange processes[1,2]. For example, M. Osada et al. reported a $Ca_2Nb_3O_{10}$ (CNO) dielectric nanosheet which can be fabricated through a two-step cation exchange processes, and they reported its high dielectric permittivity (ε_r = 200) even with a 5 nm thickness[3]. A CNO colloidal nanosheet was obtained by exfoliation which included K^+ ions exchange to H^+ ions from $KCa_2Nb_3O_{10}$ and then exfoliation by TBAOH intercalation from $HCa_2Nb_3O_{10}$.

Likewise, various types of dielectric nanosheets such as $Sr_2Nb_3O_{10}$ (SNO), which shows dielectric permittivity above 240, have been reported[4]. These dielectric nanosheets demonstrated dielectric responses with thicknesses below 20 nm; thus, these materials show boundless potential for use as next-generation dielectric alternatives. However, the dielectric properties of layered perovskite bulk materials have been rarely investigated so far. The dielectric properties of bulk $KCa_2Nb_3O_{10}$

have been reported that showed the dielectric permittivity of 46 and the dielectric loss (D) of 0.009 at 100 KHz when it was sintered at 1375 ^{o}C. Also, in the case of $HCa_2Nb_3O_{10}$ ceramic materials, the dielectric permittivity and dielectric loss were ~30 and ~0.5 at 100 kHz, respectively, when it was sintered at 800 ^{o}C[5,6]. This reported dielectric permittivity is insufficient for application in dielectric devices, and the dielectric loss of $HCa_2Nb_3O_{10}$ is too high for use in dielectric devices. To achieve high dielectric permittivity, substitution by more polarizable ions has been typically researched because of the very strong interrelation between ionic polarizability and dielectric permittivity[7]. Moreover, in order to understanding correlation between mother materials and nanosheets, the structural and dielectric properteis should be investigate.

Therefore, here, we synthesis and report the dielectric properties in a layered perovskite $KCa_{2(1-x)}Sr_{2x}Nb_3O_{10}$ and $HCa_{2(1-x)}Sr_{2x}Nb_3O_{10}$ ceramic solid solution system, which incorporates starting materials of CNO and SNO dielectric nanosheet compositions, in the range of x = 0 ~ 1 aimed to investigate the influence of the compositional ratio of Ca/Sr. For this purpose, the structural and dielectric properties of the ceramic materials have been studied, and we achieved very good dielectric properties, that is, the dielectric permittivity of over 500 and the dielectric loss below 0.09 at 100 kHz. Also, we synthesized $Ca_{0.8}Sr_{1.2}Nb_3O_{10}$ nanosheets, which show great dielectric properties and colloidal concentration, from $KCa_{0.8}Sr_{1.2}Nb_3O_{10}$ ceramic and deposited thin films on a Pt/Ti/SiO_2/Si substrate by EPD method. The structural and dielectric properties of thin films were investigated.

2.2. Experimental section

2.2.1. Synthesis of $KCa_{2(1-x)}Sr_{2x}Nb_3O_{10}$ ceramics

The layered perovskite, $KCa_{2(1-x)}Sr_{2x}Nb_3O_{10}$ (x = 0, 0.2, 0.4, 0.6, 0.8, 1) was prepared through a solid-state reaction by using K_2CO_3 (≥99%, Aldrich, USA), $CaCO_3$ (≥99%, Aldrich, USA), Nb_2O_5 (≥99.9%, Aldrich, USA), and $SrCO_3$ (≥99.9%, High Purity Chemistry, Korea) in stoichiometric proportions as raw materials. The raw materials were ball-milled in anhydrous ethyl alcohol (≥99.99%, Aldrich) for 20 hours and dried at 100 ^oC for 10 hours. Afterwards the mixture was ground and calcined at 1200 ^oC for 10 hours in air. Then, the layered perovskite $KCa_{2(1-x)}Sr_{2x}Nb_3O_{10}$ powders were synthesized, and the obtained powders (5 g) were continuously stirred in 5-7 M HNO_3 solution (200 ml) using a mechanical stirrer for 4 days at room temperature to get $HCa_{2(1-x)}Sr_{2x}Nb_3O_{10}$ (x = 0, 0.2, 0.4, 0.6, 0.8, 1). Through this process, the K^+ ions in those modified niobates were substituted by H+ ions. After replacement of the H+ ions, the products were washed several times to neutralize them and were dried at 50 ^oC in an oven overnight.

2.2.2. Structural and dielectric properties measurements

The synthesized $KCa_{2(1-x)}Sr_{2x}Nb_3O_{10}$ and $HCa_{2(1-x)}Sr_{2x}Nb_3O_{10}$ powders were compressed into disc shaped pellets of 12 mm in diameter under a pressure of 100 kgf/cm^2, and these pellets were polished to form disk with 0.5–1 mm thickness. Then, the pellets were sintered at 1250 ^oC for 2 hours in a furnace under an air atmosphere. After that, the sintered pellets were polished on both side, and a silver electrode was screen printed on both sides and fired at 600^oC for 10 min to ensure good electrical contact for the estimation of dielectric properties.

X-ray diffraction (XRD) studies were carried out for phase identification. The XRD patterns were obtained using small-angle X-ray spectroscopy (D/MAX-2500, Rigaku, Japan) with Cu Kα radiation. Also, the infrared (IR) spectra were measured

from the KBr pellets in transmission mode using FT-IR spectrometry (Nicolet iS10, Thermo scientific, USA). The KBr circular pellets were prepared in an air atmosphere by compression from a mixture of KBr (FT-IR grade, Aldrich, USA) and powder of each composition. The microstructure and elementary composition of synthesized powders were observed by environmental scanning electron microscopy (ESEM) (XL-30 FEG, FEI, USA) and X-ray energy dispersive spectroscopy (EDS) (XL-30 FEG, FEI, USA). The dielectric measurements were acquired at a frequency range from 1 KHz to 1 MHz using an impedance analyzer (Agilent Technologies HP 4294A, Santa Clara, USA)

2.2.3. Synthesis of $Ca_{0.8}Sr_{1.2}Nb_3O_{10}$ (CSNO) nanosheets

The CSNO nanosheets were prepared by delamination of the layered perovskite compound $HCa_{0.8}Sr_{1.2}Nb_3O_{10}$. The precursor powder was dispersed in a tetrabutylammonium hydroxide (TBAOH) solution and continuously shaken at room temperature for 7 days to exfoliate each $Ca_{0.8}Sr_{1.2}Nb_3O_{10}$ layer. The $Ca_2Nb_3O_{10}$ nanosheets were prepared in same way as a comparison material for comparison. Both nanosheets were deposited on $Pt/Ti/SiO_2/Si$ substrate by the electrophoretic deposition (EPD) method in acetone medium. The electrical voltage of 40 V was applied for 30 seconds at room temperature. After deposition thin film, ultraviolet light was irradiated to decompose residual TBA^+ ions. The dielectric properties were measured by impedance analyzer (4294A, Agilent) with platinum top electrode deposited by DC sputtering. The crystal structure was carried out through X-ray diffraction, and microstructure of thin films were obtained by scanning electron microscope (SEM) images and transmittance electron microscopy (TEM).

2.3. Results and discussion

2.3.1. Syntheses and structural characterization of $KCa_{2(1-x)}Sr_{2x}Nb_3O_{10}$ and $HCa_{2(1-x)}Sr_{2x}Nb_3O_{10}$ ceramics.

The X-ray diffraction (XRD) patterns for the series of layered perovskite $KCa_{2(1-x)}Sr_{2x}Nb_3O_{10}$ are presented in Fig. 2.1 (a), and the patterns indicate that homogeneous phase powders are formed without any other phase by solid-state reaction. The diffraction peaks gradually shifted to a lower angle with an increasing Sr component ratio, indicating an increased interlayer because Sr ions are larger than Ca ions. Also, the diffraction peaks show that Sr ions can be fully substituted to Ca ions without the appearance of any second phase.

A similar tendency was observed in the XRD patterns of proton intercalated $HCa_{2(1-x)}Sr_{2x}Nb_3O_{10}$ powders as shown in Fig. 2.1 (b). By comparison XRD patterns, there were lower angle shifts in all of the main peak positions after proton exchange, which indicates increase of the c axis because of protons entering the lattice as hydrated proton ions ($H3O^+$)[8,9].

Also, the exchange of larger diameter hydrated proton ions rather than smaller proton ions was double checked by IR spectroscopy. The IR spectroscopy results of the samples are presented in Fig. 2.2 (a) $KCa_{2(1-x)}Sr_{2x}Nb_3O_{10}$ and (b) $HCa_{2(1-x)}Sr_{2x}Nb_3O_{10}$ systems. The peaks around 925, 769, and 590 cm^{-1} represent three bands of Nb-O vibrations; the 925 cm^{-1} peak is assigned to the terminal Nb-O vibrational stretching[10]; the 769 cm^{-1} peak is assigned to the asymmetric stretching vibration (Nb-O-Nb) of bridge Nb-O in terminal distorted NbO_6 octahedron; and the 590 cm^{-1} peak is attributed to the asymmetric stretching vibration of bridge Nb-O in central NbO_6 octahedron, which is undistorted[11,12]. The IR spectra of $HCa_{2(1-x)}Sr_{2x}Nb_3O_{10}$ went through a 26 cm^{-1} red shift due to increasing interactions between cations and the terminal Nb-O bonds, and this interaction difference is caused by distinctive

coordination sites according to the size of cation. All peak position of Nb-O vibrations in both $KCa_{2(1-x)}Sr_{2x}Nb_3O_{10}$

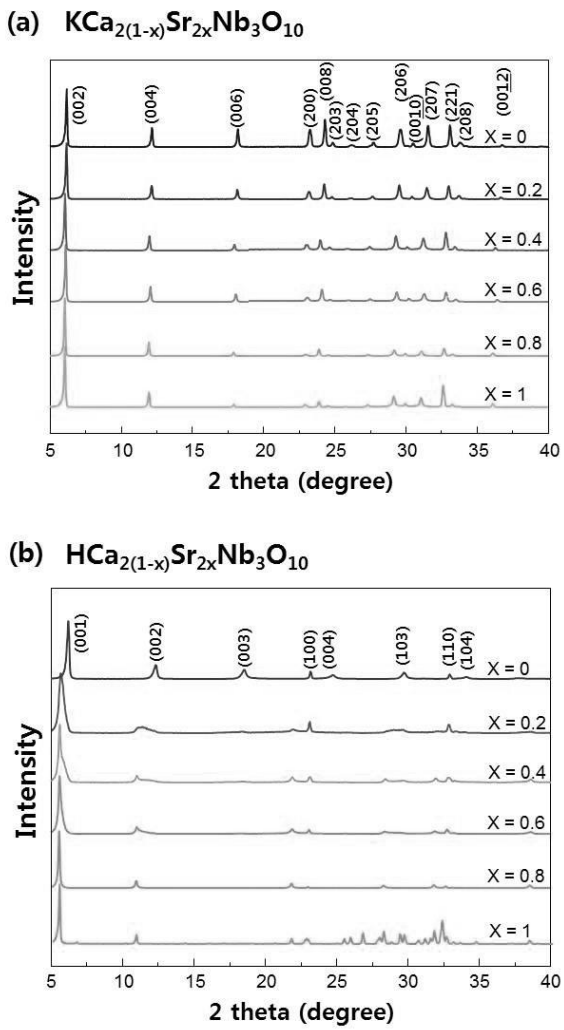

Figure 2.1. X-ray diffraction patterns of niobate powders: (a) patterns from $KCa_{2(1-x)}Sr_{2x}Nb_3O_{10}$ correspond to the perovskite layered structure (JCPDS 97-015-7839, $KCa_2Nb_3O_{10}$); (b) patterns from $HCa_{2(1-x)}Sr_{2x}Nb_3O_{10}$ are also well matched (JCPDS 00-040-0884, $HCa_2Nb_3O_{10}$); (c) patterns from $[H]Ca_{2(1-x)}Sr_{2x}Nb_3O_{10}$, which was sintered for pelletizing, are indexed with two phases of $Ca_2Nb_2O_6$(JCPDS 97-002-6010) and $CaNb_2O_6$(JCPDS 97-001-5208).

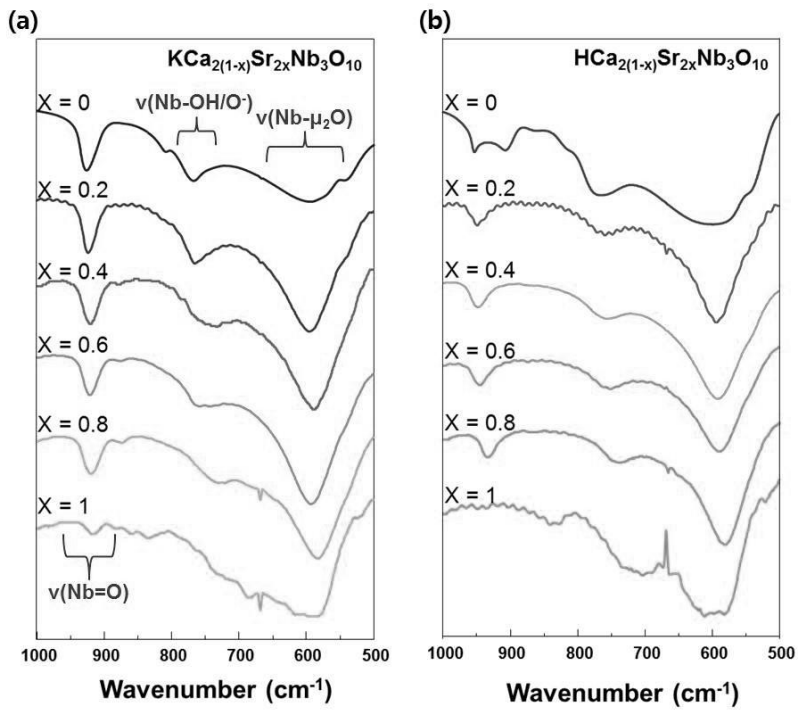

Figure 2.2. Infra-red spectra of (a) $KCa_{2(1-x)}Sr_{2x}Nb_3O_{10}$ and (b) $HCa_{2(1-x)}Sr_{2x}Nb_3O_{10}$ powders between 1000 and 500 cm^{-1}.

and $HCa_{2(1-x)}Sr_{2x}Nb_3O_{10}$ slightly shifted toward a higher wavelength as increasing Sr contents correspond with larger Sr ions as compared to Ca ions.

The morphological analysis of the synthesized $KCa_{2(1-x)}Sr_{2x}Nb_3O_{10}$ and $HCa_{2(1-x)}Sr_{2x}Nb_3O_{10}$ powders were investigated by SEM, and the results are shown in Fig. 2.3; both samples clearly show a lamella structure that included perovskite layers formed by cations. The layered microcrystal structure of $KCa_{2(1-x)}Sr_{2x}Nb_3O_{10}$ was maintained even after substitution with strontium, and the layered structure of protonic formed niobate, which is in the formula of $KCa_{2(1-x)}Sr_{2x}Nb_3O_{10}$, was retained as well. The particle size of the niobate powders increased with increase in the amount of the Sr component; the grain sizes of the powder increased in range from ~ 3 μm to above 5 μm with additional strontium fraction.

The EDS patterns of the synthesized $KCa_{2(1-x)}Sr_{2x}Nb_3O_{10}$ and $HCa_{2(1-x)}Sr_{2x}Nb_3O_{10}$ are shown in Fig. 2.4. Through acid treatment K^+ intercalated $KCa_{2(1-x)}Sr_{2x}Nb_3O_{10}$ to H^+ intercalated niobate, the peak around 330 keV, which is indexed to the K^+ ions, disappeared. This indicates that K^+ ions are fully exchanged in $HCa_{2(1-x)}Sr_{2x}Nb_3O_{10}$ forms. With the substitution of the Ca component for the Sr component, the 370 and 404 keV peaks of Ca faded, and the peaks of 160 and 181 KeV appeared, corresponding to Sr.

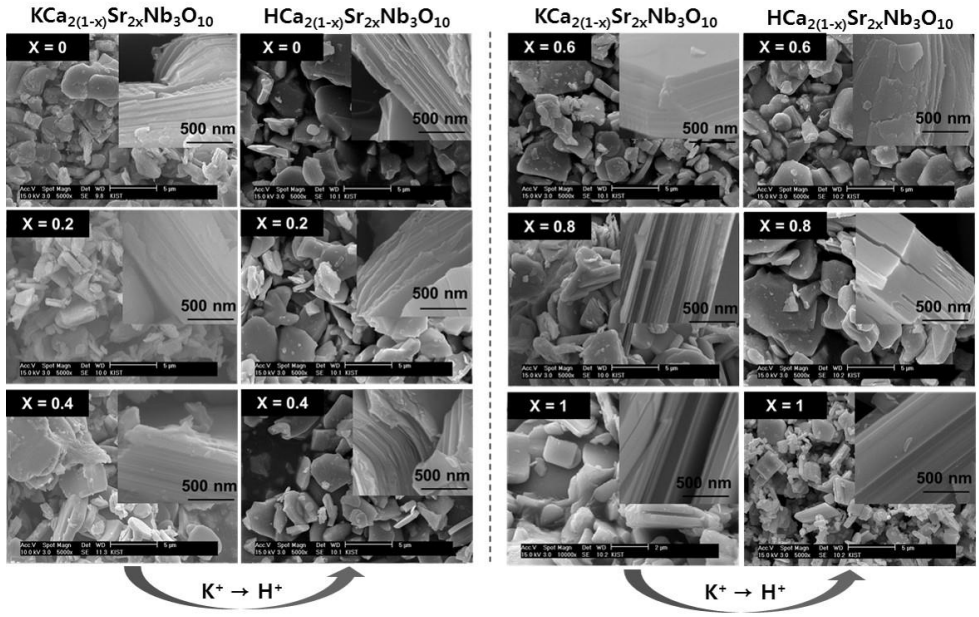

Figure 2.3. SEM micrographs of (a) $KCa_{2(1-x)}Sr_{2x}Nb_3O_{10}$ and (b) $HCa_{2(1-x)}Sr_{2x}Nb_3O_{10}$ powders.

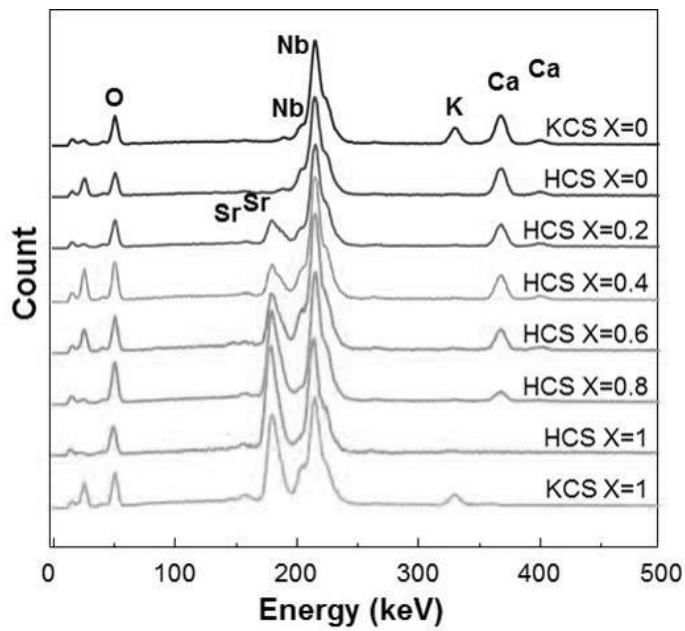

Figure 2.4. EDS elemental analysis results of (a) $KCa_{2(1-x)}Sr_{2x}Nb_3O_{10}$ and (b) $HCa_{2(1-x)}Sr_{2x}Nb_3O_{10}$ powders.

2.3.2. Dielectric characterization of $KCa_{2(1-x)}Sr_{2x}Nb_3O_{10}$ and $HCa_{2(1-x)}Sr_{2x}Nb_3O_{10}$ ceramics.

The To measure the dielectric properties of the synthesized powders, sintering was carried out at 1250 °C, and the $KCa_{2(1-x)}Sr_{2x}Nb_3O_{10}$ series maintained the same phase after sintering. However, in the case of the $HCa_{2(1-x)}Sr_{2x}Nb_3O_{10}$ series, the mixture of stable $Ca_{1-x}Sr_xNb_2O_6$ and $Ca_{2(1-x)}Sr_{2x}Nb_2O_7$ phase formed during the sintering process by the following reaction like the well-known $HCa_2Nb_3O_{10}$[6]:

$$2HCa_{2(1-x)}Sr_{2x}Nb_3O_{10} \rightarrow H_2O + Ca_{4(1-x)}Sr_{4x}Nb_6O_{19}$$

$$Ca_{4(1-x)}Sr_{4x}Nb_6O_{19} \rightarrow 2Ca_{(1-x)}Sr_xNb_2O_6 + Ca_{2(1-x)}Sr_{2x}Nb_2O_7$$

The X-ray diffraction patterns relevant to these phase transition in $2Ca_{(1-x)}Sr_xNb_2O_6$-$Ca_{2(1-x)}Sr_{2x}Nb_2O_7$ mixtures are shown in Fig. 2.5 (a), and their thermal properties, as determined by thermogravimetry (TG) and differential thermal analysis (DTA) are shown in Fig. 2.5 (b). The weight of the samples gradually decreased to 100 °C because of the small amount of residual water, and the weight loss at 320 °C is seen with exothermic peak assignment resulting from the formation of H_2O and $Ca_{4(1-x)}Sr_{4x}Nb_6O_{19}$ from $2HCa_{2(1-x)}Sr_{2x}Nb_3O_{10}$. In relation to the applied heat, disproportionation reaction began at 800 °C without mass loss, which is the proof of disproportionation reaction from $Ca_{4(1-x)}Sr_{4x}Nb_6O_{19}$ to $2Ca_{1-x}Sr_xNb_2O_6$ and $Ca_{2(1-x)}Sr_{2x}Nb_2O_7$ phase[13].

The dependence on the amount of strontium substitution in the dielectric permittivity and dielectric loss in the range from 1 KHz to 1 MHz is shown in Fig. 2.6 Depending on the value of x, the dielectric permittivity in $KCa_{2(1-x)}Sr_{2x}Nb_3O_{10}$. and $2Ca_{(1-x)}Sr_xNb_2O_6$-$Ca_{2(1-x)}Sr_{2x}Nb_2O_7$ mixtures are strongly impacted; the dielectric constant of both $KCa_{2(1-x)}Sr_{2x}Nb_3O_{10}$. and $2Ca_{(1-x)}Sr_xNb_2O_6$-$Ca_{2(1-x)}Sr_{2x}Nb_2O_7$ mixtures increased with increasing Sr ratio; and these results indicate the substitution of Sr^{2+} ions for Ca^{2+} ions due to the large ionic polarizability of Sr^{2+} ions in the lattice.

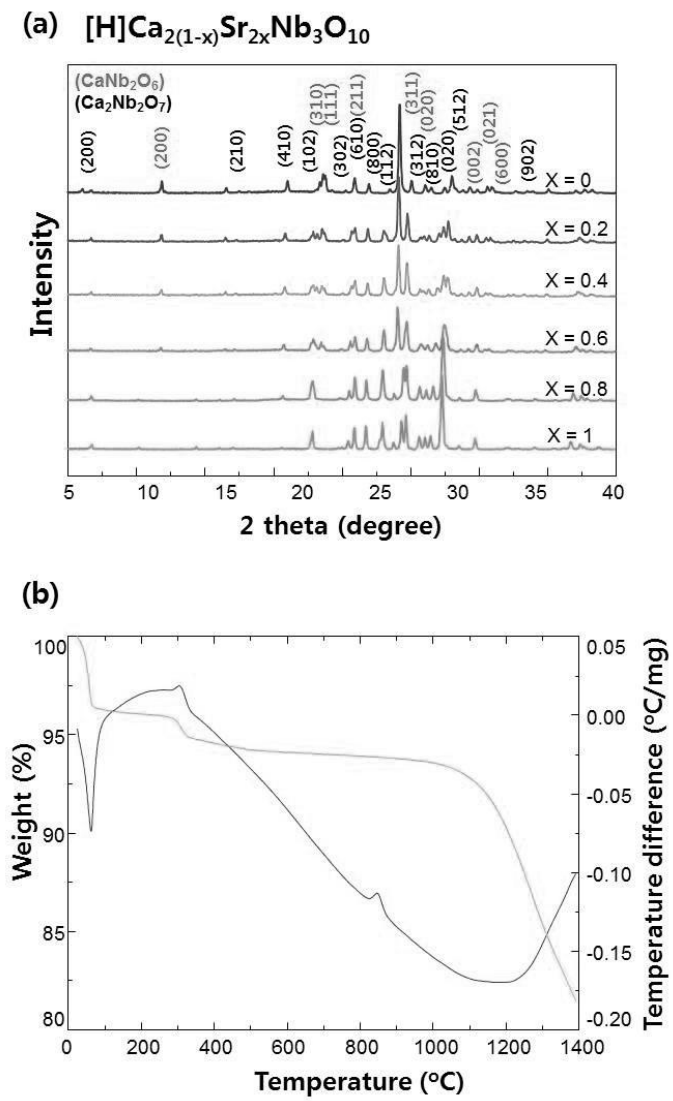

Figure 2.5. (a) XRD, (b) differential thermal analysis (DTA) and termogravimetry (TG) analysis results of $HCa_{2(1-x)}Sr_{2x}Nb_3O_{10}$ powders.

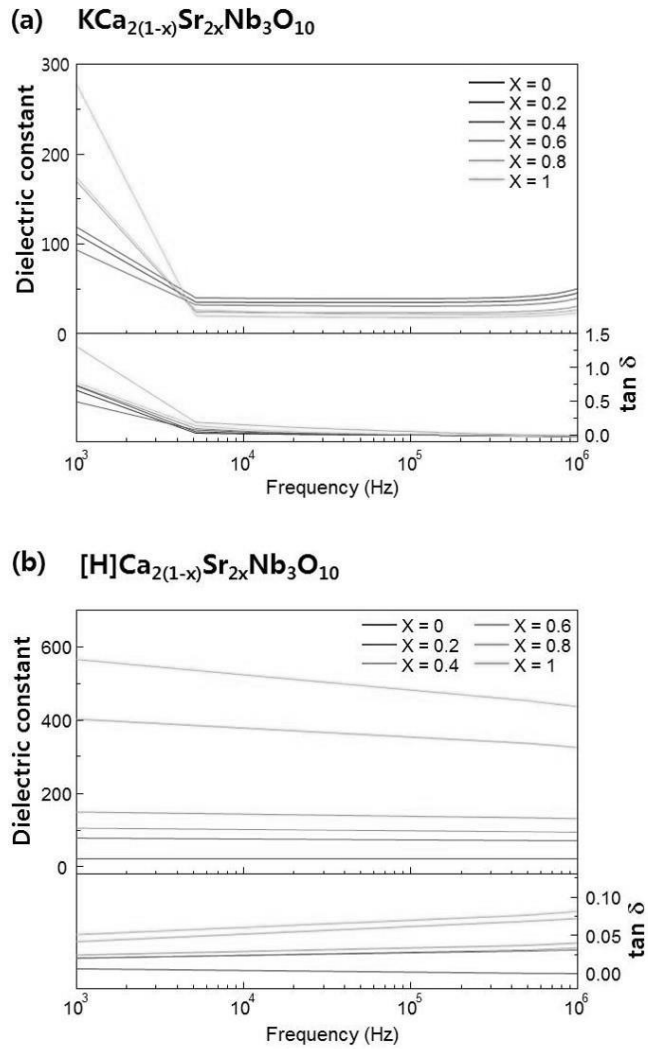

Figure 2.6. Dielectric constant (ε_r) and loss (tan δ) of (a) $KCa_{2(1-x)}Sr_{2x}Nb_3O_{10}$ and (b) $[H]Ca_{2(1-x)}Sr_{2x}Nb_3O_{10}$ ceramics as a function of frequency.

The dielectric permittivity of $KCa_{2(1-x)}Sr_{2x}Nb_3O_{10}$ gradually decreased with increasing frequency, and low dispersion was observed at frequencies > 5 KHz, where the effects of space charge and interfacial polarization are diminished. On the other hand, the dielectric permittivity of $2Ca_{(1-x)}Sr_xNb_2O_6$-$Ca_{2(1-x)}Sr_{2x}Nb_2O_7$ mixtures was higher than that of $KCa_{2(1-x)}Sr_{2x}Nb_3O_{10}$ with low dispersion irrespective of the frequency range. This is because of the properties from two phase of $Ca_{1-x}Sr_xNb_2O_6$ and $Ca_{2(1-x)}Sr_{2x}Nb_2O_7$ phase, which coexist in the sintered $HCa_{2(1-x)}Sr_{2x}Nb_3O_{10}$ pellets as seen in Fig. 2.6, and show a constant dielectric permittivity[14] due to the absence of protons with crystallization to a two-phase compound.

The compositional dependence of the Raman spectra of $KCa_{2(1-x)}Sr_{2x}Nb_3O_{10}$ is shown in Fig. 2.7, and it is divided into a high-frequency mode and low-frequency mode fiducially 200 cm^{-1} mode. As shown in Fig. 2.7 (b), with increasing substitution of Sr contents, the ν = 210 cm^{-1} mode appears, which is related to the vibration of Sr^{2+} cations in the layer[15]. In addition, the mode shows smaller shift mostly when substituted cations are heavier[16]; therefore, the smaller shifted peaks of the 210 cm^{-1} mode in relation to Sr^{2+} substitution indicate that light Ca^{2+} cations are well substituted by heavy Sr^{2+} cations. The strong responses of NbO_6 octahedra are observed; the 310 cm^{-1} mode of ν_5 (F_{2g})[17] expresses the bending modes; the 540 cm^{-1} mode of ν_2 (E_g) and the 800 cm^{-1} mode of ν_1 (A_{1g}) express the symmetry modes of Nb-O stretching[18,19], respectively. The ν_5 (F_{2g}), ν_2 (E_g), and ν_1 (A_{1g}) modes are moved to a lower wavenumber by the substitution of Sr^{2+} for Ca^{2+}.

Also, gradually increased dielectric permittivity with increasing Sr contents is indicated by low-frequency mode Raman analysis below 200 cm^{-1}; generally, the polarizability of perovskite material is established by the balance between the ionic bonding and covalent bonding in the BO_6 octahedra, and the lowest-frequency mode is related to the coordinated dipole interactions of the perovskite layer[20]. In Fig. 2.7 (a), the low-frequency mode shows smaller shift, and it signifies the decreasing

hardening soft-mode vibration. Accordingly, this change clearly suggests higher polarizability of the lattice and leads to an increased dielectric response. Therefore, substitution of Sr^{2+} ions in the $Ca_2Nb_3O_{10}$ system has potential for dielectric materials.

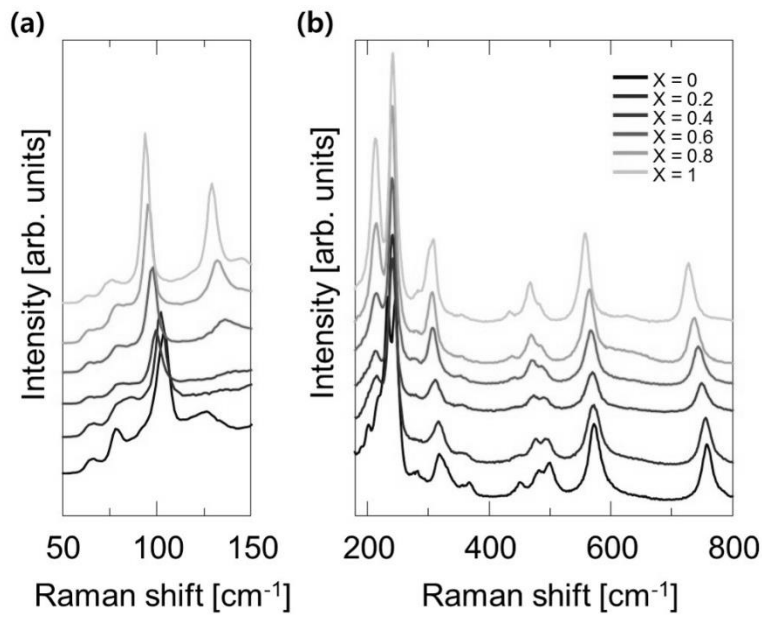

Figure 2.7. Raman spectrum of $KCa_{2(1-x)}Sr_{2x}Nb_3O_{10}$ ceramics in (a) low-frequency and (b) high-frequency modes.

2.3.3. Dielectric characterization of $Ca_{0.8}Sr_{1.2}Nb_3O_{10}$ nanosheets thin films

Among the $Ca_{2(1-x)}Sr_{2x}Nb_3O_{10}$ nanosheets, we deposited thin film with $Ca_{0.8}Sr_{1.2}Nb_3O_{10}$ nanosheets, which shows great dielectric properties in bulk form with great fabrication yield, by electrophoretic deposition method. Unlike the complex and time-consuming layer-by-layer deposition (LBL) or Langmuir-Blodgett (LB), electrophoretic deposition (EPD) method has the advantage to simply obtain uniform dielectric thin films. In addition, it is possible to directly control the thickness of the dielectric film by adjusting the deposition time[21,22] and electric potential[23]. Even the dielectric constant of EPD depositied samples shows lower value than LB deposited thin films due to its worse crystallinity[24], EPD relizes very simple and fast fabrication. Therefore, in order to more easily identify trends in changes in dielectric properties dielectric properteis, we deposited thin films by EPD method.

Proton intercalated $HCa_2Nb_3O_{10}$ and $HCa_{0.8}Sr_{1.2}Nb_3O_{10}$ ceramics were dispersed in a TBAOH solution and shaken 7 days. Then, incorporation of TBA^+ ions to H^+ ions make expand the each perovskite layer as shown in Fig. 2.8 (a). Finally, the $Ca_{0.8}Sr_{1.2}Nb_3O_{10}$ (CSNO) and $Ca_2Nb_3O_{10}$ (CNO as a comparison material) solution was stabilized by centrifuging at 2000 rpm for 10 min.

The morphological properties of chemically exfoliated CSNO nanosheets were obtained by TEM observation in Fig. 2.8 (b), and the lateral size of the CSNO nanosheets were estimated over 100 nm. Fig. 2.8 (c) presents the SEAD pattern of CSNO nanosheet. It clearly indicated the single crystal nature of nanosheet along the [001] direction. Using obtained colloidal nanosheets, we deposited dielectric thin film by EPD method on $Pt/Ti/SiO_2/Si$ substrate. Fig. 2.9 (a) and (b) show the top and cross-sectional SEM image is CNO and CSNO thin film. To grow thin films, the electrical voltage of 40 V was applied for 30 seconds. In this condition, the thickness

of CNO and CSNO thin film is about 830 nm and 350 nm, and the uniform and smooth surface thin films can be deposited as shown in SEM images.

The thickness of the two sample is difference in same deposition condition because the thickness is dependent on concentration of solution. We assume that the different density of precursor pellet causes the difference cation exchanging degree and concentration. After fabrication of dielectric thin films, the platinum dots were deposited by DC sputtering as a top electrode to measure dielectric properties.

The dielectric properties of 830 nm CNO and 350 nm CSNO films are shown in Fig. 2.10 (a) and (b) according to the frequency. The dielectric permittivity (ε_r) of CNO and CSNO thin films exhibited 32 and 64 at 1 kHz. The CSNO thin films shows twice higher dielectric permittivity than CNO thin film, and this results follow the properties of precursor. The more polarizable Sr^{2+} ions increase the dielectric permittivity. As increasing the measuring frequency, the both ε_r values are slightly decreased 29 and 52 at 1 MHz. This tendency is caused by the effects of space charge and interfacial polarization from residual TBA^+ ions. The tan δ of both thin films were exhibited under 0.15 in all frequency range. Therefore, the enhanced dielectric thin films can be obtained by simple EPD deposition method as using A-site substituted CNO nanosheets with Sr^{2+} ions and it can be used as a new material to fabricate dielectric thin films.

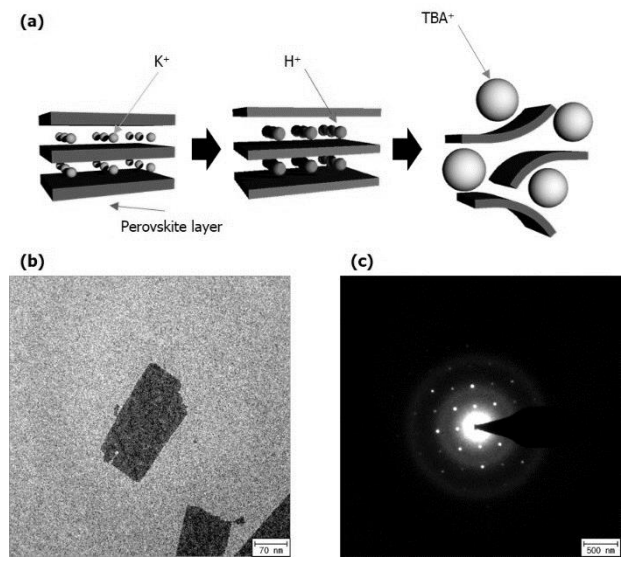

Figure 2.8. (a) A schematic diagram of cation exchange process, (b) TEM image and (c) SEAD pattern of $Ca_{0.8}Sr_{1.2}Nb_3O_{10}$ nanosheet.

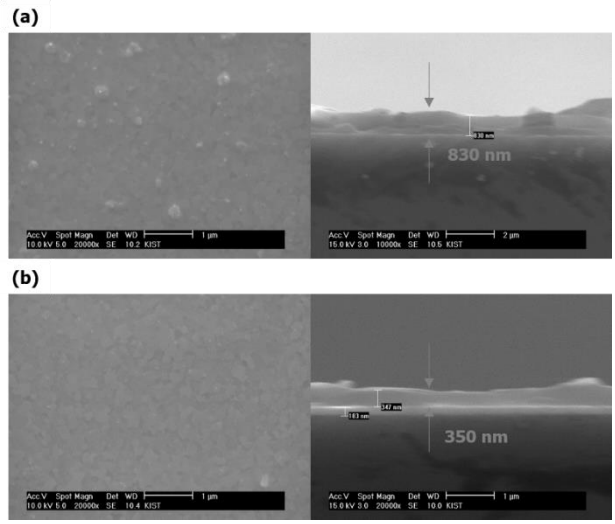

Figure 2.9. Top and Cross-sectional SEM images of (a) $Ca_2Nb_3O_{10}$ thin film and (b) $Ca_{0.8}Sr_{1.2}Nb_3O_{10}$ thin film.

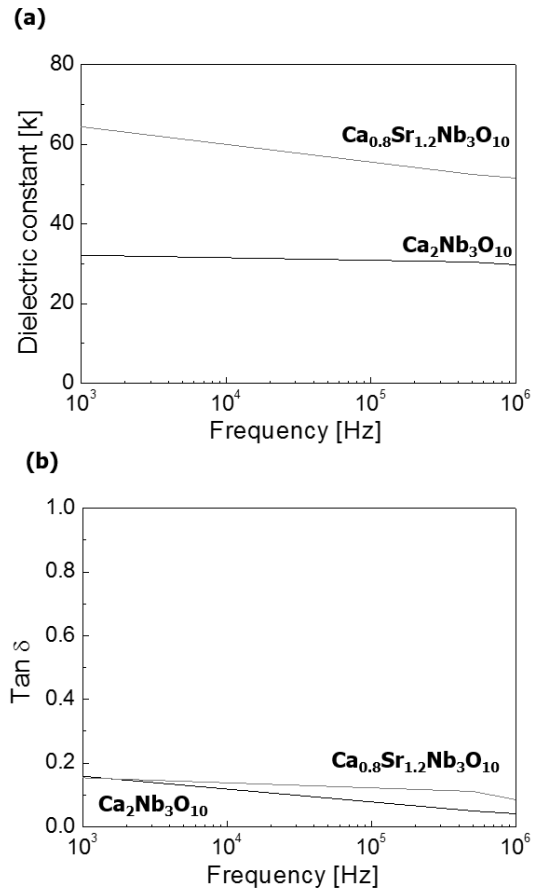

Figure 2.10. Dielectric properties of $Ca_2Nb_3O_{10}$ and $Ca_{0.8}Sr_{1.2}Nb_3O_{10}$ thin films.

2.4. Conclusions

Layered perovskite $KCa_{2(1-x)}Sr_{2x}Nb_3O_{10}$ (x = 0, 0.2, 0.4, 0.6, 0.8, 1) was synthesized by a conventional solid-state method, and $HCa_{2(1-x)}Sr_{2x}Nb_3O_{10}$ (x = 0, 0.2, 0.4, 0.6, 0.8, 1) was obtained using a cation exchange method. The single phase of the layered perovskite structure was confirmed by XRD and SEM, and well exchanged proton intercalation compounds were investigated using EDS, IR, and Raman. We measured the dielectric characteristics of strontium substituted calcium niobate ceramics and found that the dielectric response improved as a consequence of substitution of Sr^{2+} cations for Ca^{2+} cations. Also, the dielectric responses of the synthesized materials were compared. The $2Ca_{(1-x)}Sr_xNb_2O_6$-$Ca_{2(1-x)}Sr_{2x}Nb_2O_7$ mixtures series showed higher and invariant dielectric permittivity with lower dielectric loss according to the frequency change. Moreover, the $Ca_{0.8}Sr_{1.2}Nb_3O_{10}$ colloidal nanosheets were successfully synthesized through 2-step cation exchanging process and deposited on $Pt/Ti/SiO_2/Si$ substrate as thin film by electrophoretic deposition method which enable fast and simple deposition. The thickness of CSNO thin film was about 350 nm and exhibited twice higher dielectric permittivity (ε_r = 64 at 1 kHz and 52 at 1 MHz). Therefore, these layered perovskite compounds have potential as dielectric materials for electronic components.

3.5. References

[1] R. E. Schaak and T. E. Mallouk, *Chem Mater*, **12**, 3427 (2000).

[2] M. A. Bizeto, A. L. Shiguihara and V. R. L. Constantino, *J Mater Chem*, **19**, 2512 (2009).

[3] M. Osada, K. Akatsuka, Y. Ebina, H. Funakubo, K. Ono, K. Takada and T. Sasaki, *Acs Nano*, **4**, 5225 (2010).

[4] B. W. Li, M. Osada, K. Akatsuka, Y. Ebina, T. C. Ozawa and T. Sasaki, *Jpn J Appl Phys*, **50** (2011).

[5] M. M. Fang, C. H. Kim and T. E. Mallouk, *Chem Mater*, **11**, 1519 (1999).

[6] S. H. Kweon, M. Im, G. Han, J. S. Kim, S. Nahm, J. W. Choi and S. J. Hwang, *J Eur Ceram Soc*, **33**, 907 (2013).

[7] E. Cockayne, *J Appl Phys*, **103** (2008).

[8] C. S. Sun, P. Peng, L. R. Zhu, W. J. Zheng and Y. N. Zhao, *Eur J Inorg Chem*, 3864 (2008).

[9] Z. H. Zhong, W. P. Ding, Y. Chen, X. Y. Chen, Y. Y. Zhu and N. B. Min, *Appl Phys Lett*, **75**, 1958 (1999).

[10] K. Saruwatari, H. Sato, T. Idei, J. Kameda, A. Yamagishi, A. Takagaki and K. Domen, *J Phys Chem B*, **109**, 12410 (2005).

[11] M. Dussauze, E. I. Kamitsos, E. Fargin and V. Rodriguez, *J Phys Chem C*, **111**, 14560 (2007).

[12] Y. F. Chen, X. H. Zhao, H. Ma, S. L. Ma, G. L. Huang, Y. J. Makita, X. D. Bai and X. J. Yang, *J Solid State Chem*, **181**, 1684 (2008).

[13] A. J. Jacobson, J. T. Lewandowski and J. W. Johnson, *J Less-Common Met*, **116**, 137 (1986).

[14] R. J. Cava, J. J. Krajewski and R. S. Roth, *Mater Res Bull*, **33**, 527 (1998).

[15] S. M. Huang, Y. C. Li, C. D. Feng, M. Gu and X. L. Liu, *J Am Ceram Soc*, **91**, 2933 (2008).

[16] M. Osada, M. Tada, M. Kakihana, T. Watanabe and M. Funakubo, *Jpn J Appl Phys 1*, **40**, 5572 (2001).

[17] P. Ayyub, M. S. Multani, V. R. Palkar and R. Vijayaraghavan, *Phys Rev B*, **34**, 8137 (1986).

[18] C. T. Lee, C. C. Ou, Y. C. Lin, C. Y. Huang and C. Y. Su, *J Eur Ceram Soc*, **27**, 2273 (2007).

[19] L. Sun, C. Feng, L. Chen and S. Huangz, *J Am Ceram Soc*, **90**, 3875 (2007).

[20] B. W. Li, M. Osada, Y. Ebina, T. C. Ozawa, R. Z. Ma and T. Sasaki, *Appl Phys Lett*, **96** (2010).

[21] I. Zhitomirsky, Adv Colloid Interfac, 97, 279 (2002).

[22] A. Matsuda, H. Sakamoto, M. A. B. Nor, G. Kawamura and H. Muto, J Phys Chem B, 117, 1724 (2013).

[23] L. H. Xue, K. Kajiyoshi and Y. W. Yan, Thin Solid Films, 518, 10 (2009).

[24] W. H. Lee, M. Im, S. H. Kweon, J. U. Woo, S. Nahm, J. W. Choi and S. J. Hwang, J Am Ceram Soc, 100, 1098 (2017).

Chapter 3. Synthesis and characterization of Bi-substituted $Sr_2Nb_3O_{10}$ ceramics

3.1. Introduction

In chapter 2, we confirm the change of dielectric permittivity behavior with substitution of A-site ions and correlation between mother materials and exfoliated nanosheets. In this chapter, we modified A-site of $KSr_2Nb_3O_{10}$ with Bi ions, which have a higher polarizability superior to that of Sr ions, to enhance their dielectric permittivity.

As the requirement for implementable high-k ultrathin films (< 10 nm) increases for the next-generation electronics[1], search for novel high-k materials has been persistent to further scale-down multilayer ceramic capacitors (MLCCs), gate dielectrics, and memories. Moreover, additional functionalities such as flexibility and transparency may also enable fully flexible and transparent electronics to come to reality.

In case of the conventional high-k dielectric oxides films for MLCCs such as $(Ba,Sr)TiO_3$, the thickness of dielectric layer should be reduced as much as possible in order to increase capacitance. However, synthetic spherical nano-sized powder for ultrathin film is difficult and involves much expense. Besides, the dielectric permittivity of ceramics powder are strongly affected by particle sizes and more sensitively reduced below 500 nm grain size which called the intrinsic size effect[2]. The size effect is often considered of influence a low-k interfacial dead layer from the degradation of a dielectric layer/electrode interface and the strains introduced from electrodes[3]. In addition, the film-fabrication process is required post-annealing

process which often limits the materials' application to flexible substrates. Thus, searching new direction of thin film fabrication with new type dielectric materials is urgently required for advanced devices.

Currently, two-dimensional (2D) Dion-Jacobson (DJ) phases layered perovskite nanosheets materials have been emerged as an alternative to current dielectric oxides because of their great dielectric permittivity ($\varepsilon_r > 200$) even ultrathin film region (< 10 nm), simple fabrication, chemical stability, and thermal stability. The material does not require post-annealing due to their single crystalline nature, alleviating the effect from the interfacial dead layers. The dead-layer-free nanofilms demonstrate the invariant dielectric permittivity with thickness[5]. These 2D perovskite nanosheets are obtained from DJ phases layered perovskite bulk materials described by the formula $A[A'_{n-1}B_nO_{3n+1}]$ such as $LaNb_2O_7$, $KCa_2Nb_3O_{10}$, and $KSr_2Nb_3O_{10}$. DJ phases layered materials consist of negatively charged $A'_{n-1}B_nO_{3n+1}$ perovskite slabs and occupied A cations in the interlayer space, so these materials have weak bonding between each perovskite layers. Therefore, the intercalated cation can be easily changed so that a various single crystal nanosheet can be simply delaminated into their elemental layers by exfoliating the layered structure precursors.

These simply obtained single crystal nanosheet can be assembled as thin films on a various substrate by room temperature deposition processes such as Langmuir-Blodgett[1], Layer-by-Layer process[6], and electrophoretic deposition[7]. As a result, the post annealing process is not required which causes thermal damage on dielectric thin film, so these thin films shows invariant dielectric permittivity in different thickness and can be deposited on various flexible substrate. Because of this fabulous characteristic, using two dimensional dielectric nanosheet have received enormous

attention as a new direction to fabricate nano-scaled dielectric thin film.

Several perovskite nanosheet-based thin films such as $Ca_2Nb_3O_{10}$ (ε_r = 200) and $Sr_2Nb_3O_{10}$ (ε_r = 240) have been reported[8]; yet, the reported dielectric properties fall far below those of their bulk counterpart. Therefore, here we synthesize new dielectric nanosheet materials in formula of $Sr_{2(1-x)}Bi_{2x}Nb_3O_{10}$, and we focus on not only dielectric nanosheet for thin film but also its starting materials as a microwave dielectric bulk ceramics.

3.2. Experimental section

3.2.1. Synthesis of $KSr_{2(1-x)}Bi_{2x}Nb_3O_{10}$ ceramics

In order to investigate the effect of bismuth substitution on potassium strontium niobate ceramics, the layered perovskite $KSr_{2(1-x)}Bi_{2x}Nb_3O_{10}$ (x = 0, 0.1, 0.2, 0.3) (abbreviated as KSBN 0, KSBN 0.1 KSBN 0.2, and KSAN 0.3, respectively) were prepared by solid-state reaction using K_2CO_3 (≥99%, Aldrich, USA), $SrCO_3$ (≥99.9%, High Purity Chemistry, Japan), Bi_2CO_3 (≥99%, Aldrich, USA), and Nb_2O_5 (≥99.9%, Aldrich, USA) in stoichiometric proportions as raw materials. The starting powders were ball-milled in anhydrous ethyl alcohol for 24 hours and dried at 110 ºC for 24 hours. After grinding the dried mixture, calcination was applied at temperature of 1200 ºC for 10 hours in covered alumina crucibles in the air. Then, the synthesized layered perovskite KSBN powders (5 g) were continuously stirred in 7 M HNO_3 solution (200 ml) for 5 days. During this process, the K^+ ions between $Sr_{2(1-x)}Bi_{2x}Nb_3O_{10}$ (SBN) layers were exchanged to H^+ ions and modified to $HSr_{2(1-x)}Bi_{2x}Nb_3O_{10}$ (x = 0, 0.1, 0.2, 0.3) (abbreviated as HSBN 0, HSBN 0.1 HSBN 0.2, and HSBN 0.3, respectively) ceramics. All products were washed by DI water several times to neutralize and dried at 60 ºC for 24 hr. The synthesized KSBN and HSBN powders were compressed into compact disc shaped pellets of 12 mm in diameter with polyvinyl alcohol (PVA) binder under a pressure of 100 kgf/cm^2, and the these pellets were carefully polished to form disk with 1 mm thickness after sintering at 1250 ºC for 2 hours in a furnace. And then, the polished pellets were painted by a silver electrode on both sides and fired at 600 ºC for 10 min in order to have good electrical contact for the estimation of dielectric properties.

3.2.2. Structural and dielectric properties measurements

The phase identification was carried out by X-ray diffraction (XRD) studies using Cu Kα radiation (D/MAX-2500, Rigaku, Japan), and the micro structure was

determined using scanning electron microscopy (Inspect F50, FEI, USA) while the chemical compositions of ceramics were characterized by energy dispersive X-ray spectroscopy. Fourier transform infrared spectroscopy (Nicolet iS 10, Thermo fisher scientific, USA) was carried out to obtain information of niobate bonding, and the spectra were measured from 500 to 1000 cm^{-1} at room temperature. Phase analysis was carried out with RAMAN spectra (inVia confocal Raman microscope, Renishaw plc, UK) from 100 to 800 cm^{-1}. Dielectric measurements were taken using an impedance analyzer (Agilent Technologies HP 4294A, Santa Clara, USA) in the frequency range of 1 KHz to 1 MHz at room temperature and the density of KSBN and HSBN sintering pellet was obtained by Archimedes' method.

DFT calculations were performed using the periodic supercell plane-wave basis approach, as implemented in Advance/PHASE. We used the generalized gradient approximation combined with Vanderbilt ultrasoft pseudopotentials. The wave-function was expanded in plane-waves up to a kinetic energy cutoff of 500 eV. The Brillouin-zone sampling was performed by using a $3 \times 6 \times 1$ Monkhorst-Pack grid for *k* points in a monolayer nanosheet. Structural relaxation was performed with convergence thresholds of 10^{-8} eV for the energies and 0.03 eV $Å^{-1}$ for the forces. Dielectric functions were calculated using an electric-dipole approximation.

3.2.3. Synthesis of $Sr_{1.8}Bi_{0.2}Nb_3O_{10}$ nanosheets

$Sr_{2(1-x)}Bi_{2x}Nb_3O_{10}$ (SBN) nanosheet were achieved from HSBN powders by exfoliation in tetrabuthylammonium hydroxide (TBAOH) solution with a molar ration of $TBA^+ : H^+ = 1 : 1$. The 1 g HSBN powder is shaken in 200 ml TBAOH solution for 7 days, and the mixture is centrifuged at 15000 rpm for 20 min. The insertion of large size TBA^+ cations expands the each perovskite layers and exfoliates single nanosheets. The complete exfoliated nanosheet was confirmed by Transmission electron microscope (TEM) images and a selected area electron

diffraction (SAED) pattern (Titan 80-300, FEI, USA) from the specimen that was prepared by dropping the diluted colloidal nanosheets on Cu grid. Also, the value of the zeta potential and near edge X-ray absorption fine structure was obtained.

3.3. Results and discussion

3.3.1. Syntheses and characterization of $KSr_{2(1-x)}Bi_{2x}Nb_3O_{10}$ ceramics.

We first explore the structural and dielectric properties of the starting compound in the formula of $KSr_{2(1-x)}Bi_{2x}Nb_3O_{10}$ (KSBNO). The SEM images of KSBNO ceramics are shown in Fig. 3.1 (a) and there is no microstructure variation. The average grain size of all samples is over than 5 μm, and all samples show dense fracture including lamellar structure grains without pores. According to XRD analysis in Fig. 3.1 (b), it is clearly seen that the peaks of KSBNO x= 0 to 0.2 were indexed as a single DJ phase layered perovskite structure and indicate that Bi^{3+} ions are homogeneously substituted into the Sr^{2+} lattice. During the substitution of Bi^{3+} for Sr^{2+}, we assume intercalated K^+ ions were acted to compensate for the charge changing[13]. However, a small amount of a secondary phase was presented in KSBNO (x = 0.3) sample, so the maximum substitution amount is decided to x = 0.3. Also, it seems to the intensity of the (002) and (004) peak are slightly increased as increasing Bi substitution amount while the intensity of other peaks are decreased, so these results mean the grains of (002) plane get larger according to substitute Bi content[14].

After investigating structural properties of KSBNO, we obtain of $HSr_{2(1-x)}Bi_{2x}Nb_3O_{10}$ (HSBNO) ceramic through cation exchange process in acid solution. Fig. 3.1 (c) shows the XRD patterns of HSBNO ceramics and a similar tendency is presented in the patterns. However, the all main peaks of HSBNO ceramic show lower angle shifts after cation exchange and these lower shifts ascribe the expansion of c axis by entering of hydrated proton ions (H_3O^+) instead of smaller K^+ ions[15].

The FTIR spectrum of KSBNO and HSBNO is presented in Fig. 3.2 (a) and (b). Both samples show the clear absorption peaks associated with the NbO_6 octahedron of 910 cm^{-1} which is assigned to the terminal Nb-O vibrational stretching[12], and this indicates the niobate structure is maintained well even convert K^+ ions to H^+ ions. Also, as increasing the amount of Bi component, the peaks from terminal Nb-O

vibrational stretching are gradually shifted to the lower wavelength in both samples because of smaller Bi ions as compared to Sr ions.

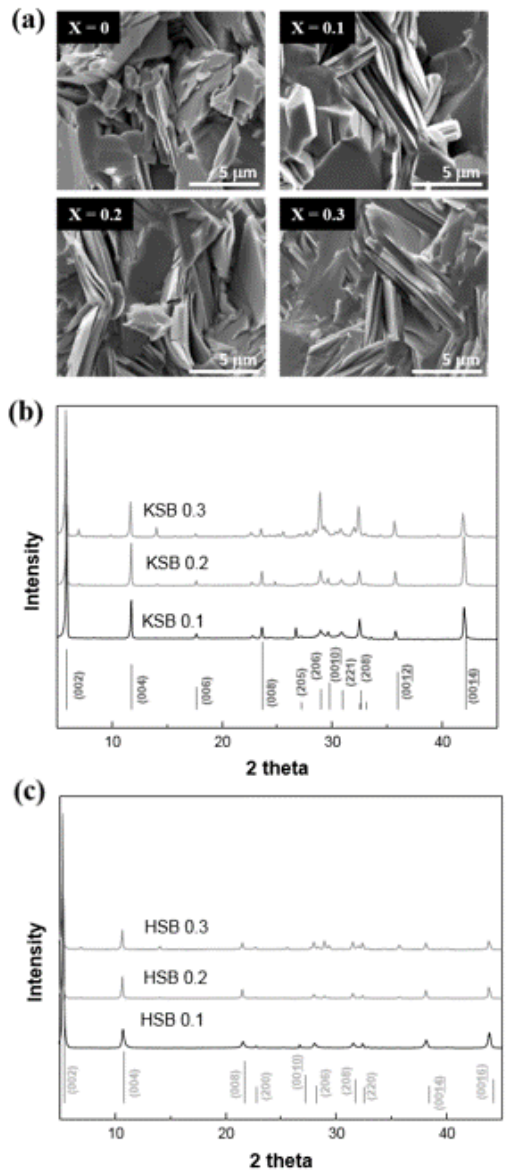

Figure 3.1. (a) SEM images of $KSr_{2(1-x)}Bi_{2x}Nb_3O_{10}$ powder (b) X-ray diffraction spectra of $KSr_{2(1-x)}Bi_{2x}Nb_3O_{10}$ ceramics and (c) X-ray diffraction spectra of $HSr_{2(1-x)}Bi_{2x}Nb_3O_{10}$ ceramics

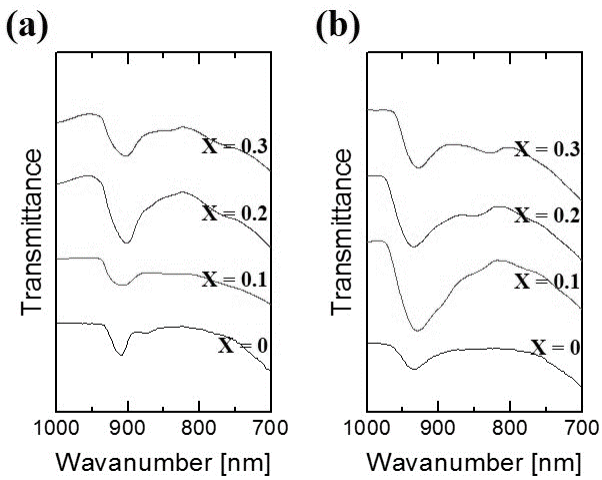

Figure 3.2. FTIR spectra of of (a) $KSr_{2(1-x)}Bi_{2x}Nb_3O_{10}$ ceramics and (b) $HSr_{2(1-x)}Bi_{2x}Nb_3O_{10}$ ceramics

3.3.2. Dielectric characterization of $KSr_{2(1-x)}Bi_{2x}Nb_3O_{10}$ ceramics.

Fig. 3.3 shows the dielectric permittivity and tan δ of KSBNO at 1250 ºC. The frequency dependence (1 kHz ~ 1 MHz) of dielectric properties were shown. As Sr ions partially substitute to Bi ions, the dielectric permittivity is increased and the dielectric loss is decreased; the dielectric permittivity of KSBNO 0 to 0.3 at 1 MHz were 31, 69, 115, and 348, respectively; the dielectric loss of KSBNO 0 to 0.3 at 1 MHz were 11.1%, 3.9%, 3.7% and 4.0%, respectively. The dielectric permittivity of all KSBN samples at 1 kHz shows higher value and decrease with the increase frequency. This low frequency dispersion is contributed by the space charge and interfacial polarization from free-charge motion effect in niobates[13,14]. The density of KSBNO is presented in Fig. 3.4. The density gradually increases with increasing Bi content; the density is measured as 3.49 g cm^{-3} in KSBNO 0 (KSNO), 4.59 g cm^{-3} in KSBNO 0.1, 4.63 g cm^{-3} in KSBNO 0.2, and 4.75 g cm^{-3} in KSBNO 0.3. The increased density might be caused by the liquid phase grain growth, due to the low melting point of Bi compounds[15]. This variation is similar with dielectric permittivity and it has been well known that higher density specimen shows lower dielectric losses due to its strong dependence on the strongly pore size and volume[,17].

The Raman measurement and the fist-principle density functional theory (DFT) calculations were performed in in Fig. 3.5 and Fig. 3.6, respectively. The vibration mode can be separated to a low frequency mode below 100 cm^{-1} and a high frequency mode above 100 cm^{-1}. The Raman spectra is sensitively changed by the structural difference and especially give polarizability of perovskite layers. The high frequency mode spectra of KSBNO give an information of niobate bonding including peaks of the internal-mode vibration of NbO_6 octahedral[16]; the 210 cm^{-1} mode is the vibration $\nu_6(F_{2u})$ which is related with the transversal vibration of K^+ and Nb^{5+}[17]; the 250 cm^{-1} mode is the vibration $\nu_5(F_{2g})$ from the bending mode; the 310 cm^{-1} mode is the vibration $\nu_4(F_{1u})$[18]; the 540 cm^{-1} mode is the vibration $\nu_2(E_g)$ symmetry

mode ; 725 cm^{-1} mode is the vibration $\nu_1(A_{1g})$ stretching modes of Nb-O bonding.

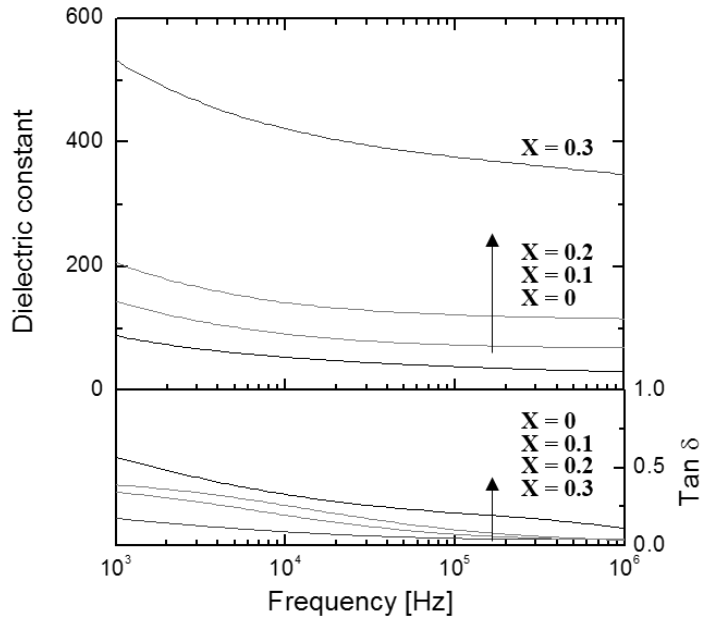

Figure 3.3. Dielectric properties of Properties of $KSr_{2(1-x)}Bi_{2x}Nb_3O_{10}$ bulk ceramics according to frequency. Each sample was pelletized with radius of 10 mm and thickness of 1 mm.

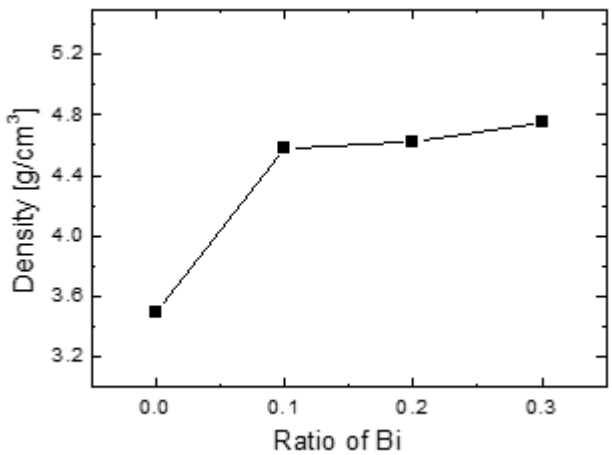

Figure 3.4. The density of $KSr_{2(1-x)}Bi_{2x}Nb_3O_{10}$ ceramics.

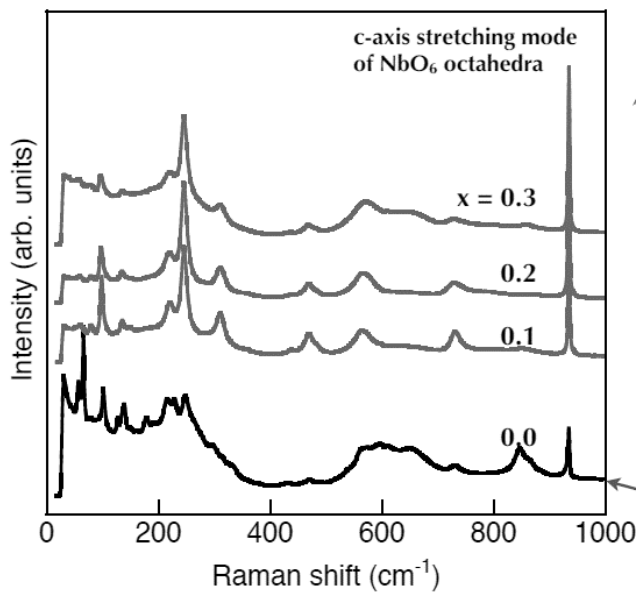

Figure 3.5. Raman scattering spectra was carried out with a Jobin-Yvon T64000 Micro-Raman system.

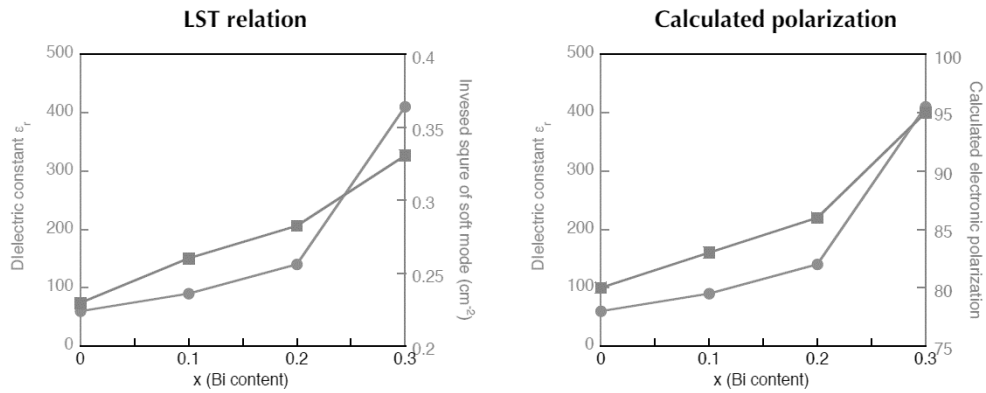

Figure 3.6. The relation of dielectric constant to inversed square of soft mode and calculated electronic polarization are presented in good agreement with the corresponding measured value.

As shown in the high frequency mode spectra, the vibration $\nu_6(F_{2u})$ shifts to the high wavenumber direction with increasing Bi substitution amount and this implies to the extension in the distortion of NbO_6 octahedral. Also, KSBNO 0 sample shows many disorder-induced modes due to the highly disordered structure, but the intensity of c-axis stretching mode in NbO_6 octahedra is enhanced while disorder-induced modes peaks are disappeared according to increasing of Bi substitution amount.

Moreover, there is a peak shift in low-frequency mode that indicate the reduction of the hardening soft-mode vibration. The balance between the ionic bonding and covalent bonding in the BO_6 octahedra generally determine the polarizability of perovskite material, and the decreased low frequency mode peaks is connected to the increased dipole interactions of the perovskite laye[10]. Thus, the decreased hardening soft-mode vibration indicate the higher polarizability and leads larger dielectric permittivity, and this observation is well-known with the other layered perovskites[18].

We can verify the relationship between macroscopic dielectric constants of materials and its microscopic properties such as soft-mode peaks (optical phonon frequencies) using Lyddane-Sachs-Teller (LST) relation. The soft modes can be detected by means of optical spectroscopy in the spectra of dielectric permittivity, and it is normally exfibited below 100-200 cm^{-1}. According to the LST relation, the static dielectric constant is proportional to the inversed square of soft-mode peaks and it is well agreed with the measured dielectric permittivity of KSBNO series; the calculated inversed square values of soft-mode peaks in KSBNO 0 to 0.3 ceramics are 0.23, 0.26, 0.28, and 0.33 cm^{-2}, respectively. Also, the computed polarization values also agree well with the measured dielectric permittivity as shown in Fig. 3.7.

3.3.3. Dielectric characterization of $HSr_{2(1-x)}Bi_{2x}Nb_3O_{10}$ ceramics.

Similar to KSBNO, the dielectric properties of HSBNO are investigated. In order to measure the dielectric properties of HSBN, the sintering process at 1250 ºC is necessary to form pellet type specimen and these high temperature process formed two stable phase. The XRD patterns and SEM images of HSBNO pellet after sintering ([H]SBNO) is presented in Fig. 3.7 (a) and (b). During the sintering process, a phase transition to the mixture of stable $Sr_{1-x}Bi_xNb_2O_6$ and $Sr_{2(1-x)}Bi_{2x}Nb_2O_7$ phase, which is presented in XRD patterns in Fig. 3.7 (a), is observed from the single-phase HSBNO ceramics by the following reaction[19].

$$2HSr_{2(1-x)}Bi_{2x}Nb_3O_{10} \rightarrow H_2O + Sr_{4(1-x)}Bi_{4x}Nb_6O_{19}$$

$$Sr_{4(1-x)}Bi_{4x}Nb_6O_{19} \rightarrow 2Sr_{(1-x)}Bi_xNb_2O_6 + Sr_{2(1-x)}Bi_{2x}Nb_2O_7$$

The main peaks from HSBNO disappeared after sintering pellet, and the main peaks in [H]SBNO are indexed on the basis of the $Sr_{1-x}Bi_xNb_2O_6$ and $Sr_{2(1-x)}Bi_{2x}Nb_2O_7$ phase. Also, according to SEM images of [H]SBNO, the grain size is 3 times smaller than that of KSBNO ceramics; this might be attributed to the breaking of grains during the cation exchange process involving magnetic stirring bar.

Fig. 3.8 shows the frequency dependence of the dielectric properties of HSBNO ceramics at room temperature. The dielectric permittivity is increased as Bi ions partially substitute to Sr ions like as KSBNO ceramics: the dielectric permittivity of HSBNO 0 to 0.3 at 1 MHz were 93, 190, 401, and 814, respectively. However, there is no significant difference in dielectric permittivity variation according to frequency unlike KSBNO due to the diminishing intercalated H^+ ions at high-temperature sintering process. The dielectric loss of HSBNO 0 to 0.3 at 1 MHz were 0.055, 0.040, 0.010 and 0.028, respectively. Also, the density of HSBNO is presented in Fig. 3.9 and shown the value of 4.4 g cm^{-3} in HSBNO 0 (HSNO), 5.0 g cm^{-3} in HSBNO 0.1, 5.2 g cm^{-3} in HSBNO 0.2, and 5.1 g cm^{-3} in HSBNO 0.3. This variation has the same tendency with dielectric loss value. Likewise KSBNO, the higher density specimen

shows the lowest dielectric losses. As a result, the maximum dielectric permittivity is 814 with a dielectric loss of 0.027 in the formula of $HSr_{1.4}Bi_{0.6}Nb_3O_{10}$ which is much better properties than previously reported values of DJ phase dielectric ceramics, so these HSBN ceramics have the potential for new generation dielectric materials.

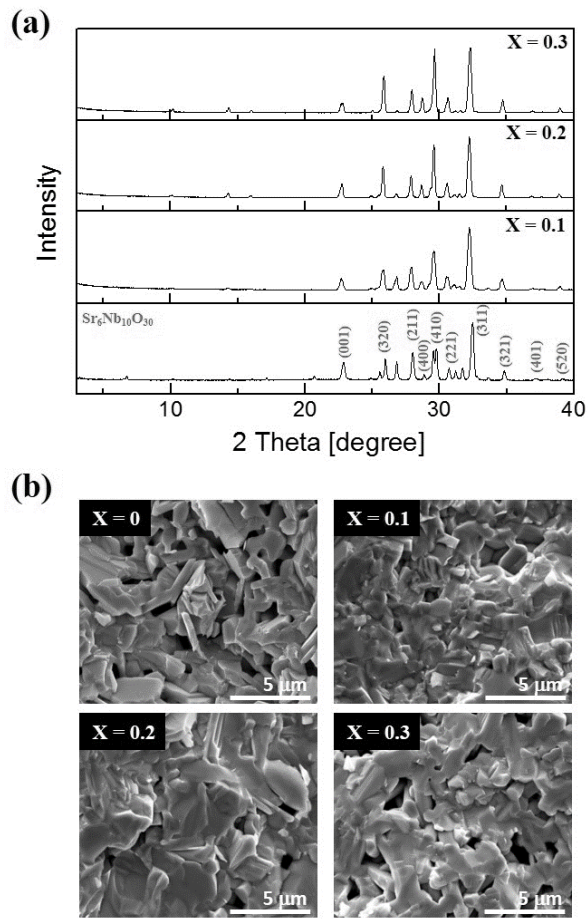

Figure 3.7. (a) X-ray diffraction spectra and (b) SEM images of [H]$Sr_{2(1-x)}Bi_{2x}Nb_3O_{10}$ ceramics ([H] indicates after sintering samples).

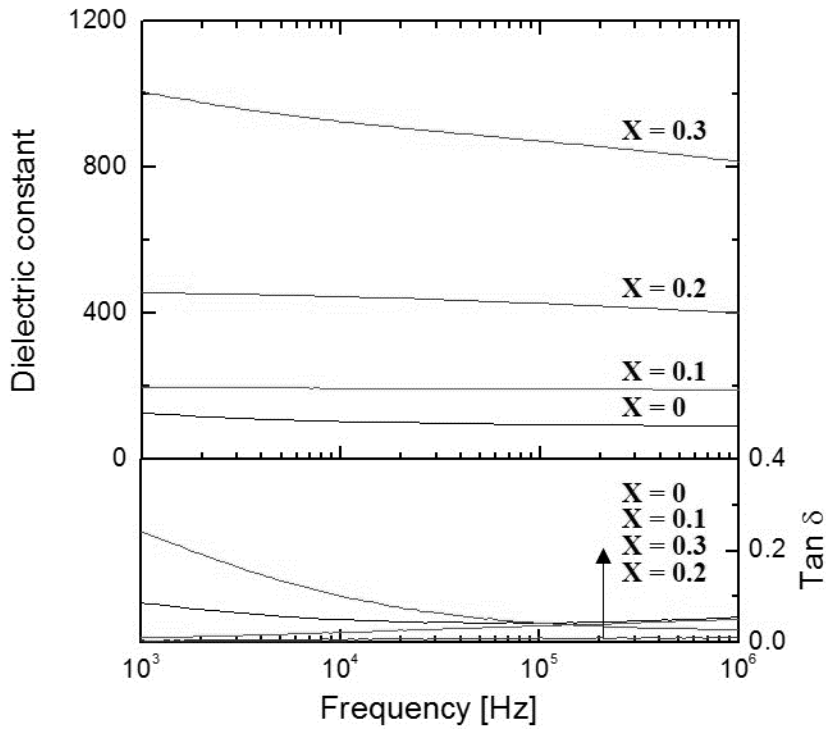

Figure 3.8. Dielectric response according to frequency of $HSr_{2(1-x)}Bi_{2x}Nb_3O_{10}$ ceramics.

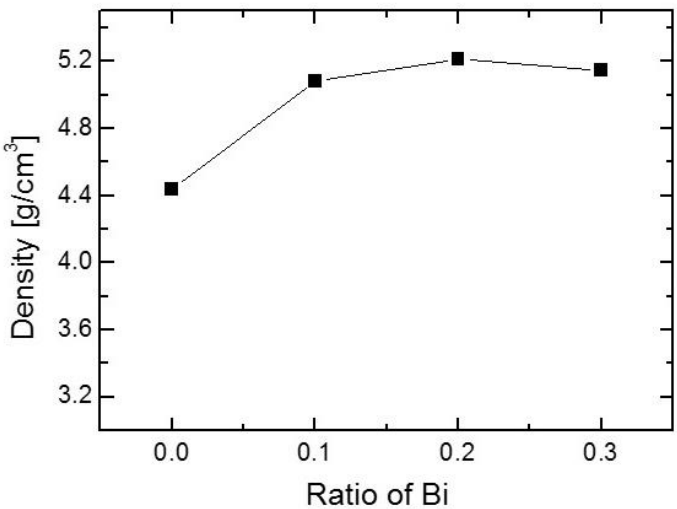

Figure 3.9. Dielectric response according to frequency of $HSr_{2(1-x)}Bi_{2x}Nb_3O_{10}$ ceramics.

3.3.4. Synthesis of $Sr_{1.8}Bi_{0.2}Nb_3O_{10}$ nanosheets.

After investigating the structural and dielectric properties of bulk materials, the negatively charged $Sr_{2(1-x)}Bi_{2x}Nb_3O_{10}$ (SBNO) nanosheets are obtained by exfoliation of layered perovskite structure HSBNO ceramics in TBAOH solution and surrounded by the positively charge TBA ions. The zeta potential of SBNO 0 (SNO) and SBNO 0.1 (x = 0.1), and SBNO 0.2 (x = 0.2) is measured as -43.9, -50.6 and -52.8 mV. This is evident that the SBN nanosheets are negatively charged and very stabilized because the zeta potential beyond 30 mV or below -30 mV is generally well known as a stable colloidal suspension in colloidal science field[20]. The colloidal suspension is highly stable over hundreds of days. However, the concentration of SBNO 0.2 collodal suspension is really low, so we are focused on SBNO 0.1 collodal suspension to analysis.

The TEM images and SAED pattern of the delaminated SBNO 0.1 nanosheets are shown in Fig. 3.10 (a), and the lateral size of the nanosheets are over hundred nanometers. The spot patterns are clearly seen square shaped and indicate that the SBNO 0.1 nanosheet has the perovskite unit cell of single crystal niobate nanosheets[21]. Fig. 3.10 (b) shows 200 kV high-angle annular dark-field scanning transmission electron microscopy (HAADF-STEM) images of SBNO 0.1 nanosheets. The A-site ions (Sr, Bi) and oxygen ions are clearly seen in the image.

Fig. 3.11 (a) shows typical AFM image of SBNO 0.1 single layer nanosheet. The thickness of SBNO 0.1 nanosheets is 1.8 nm, corresponding to three NbO_6 octahedral nano-blocks susceptible to large molecular polarizability. Fig. 3.11 (b) shows C-AFM image of SBNO 0.1 monolayer. The monolayer was incompactly deposited so that we can clearly compare the conductivity of nanosheets and the substrate. In C-AFM, an electrically conductive tip is placed in contact with the insulating nanosheet surface or conducting Pt substrate and give a topography image with current mapping with picoampere to nanoampere resolution. The nanosheets regions present

insulating property (light yellow) while the substrate regions show highly conducting property as black color.

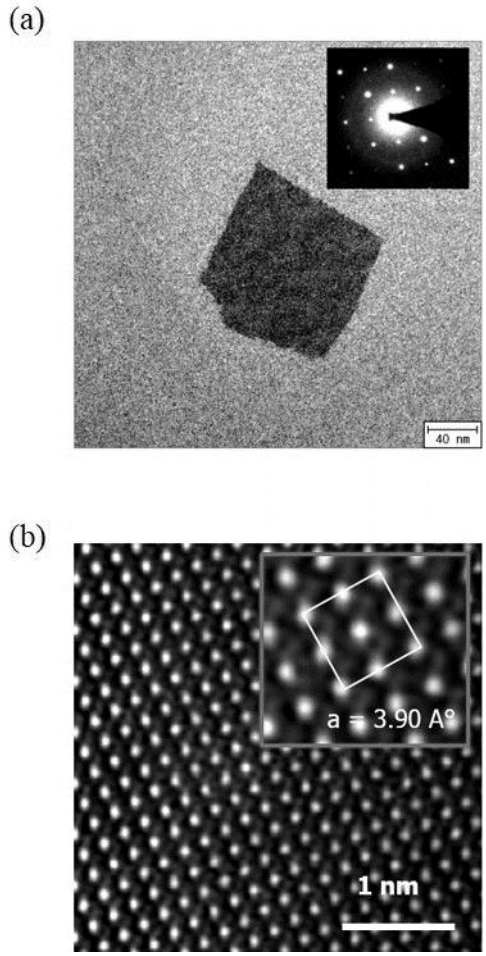

Figure 3.10. (a) TEM images of $Sr_{1.8}Bi_{0.2}Nb_3O_{10}$ nanosheet and its selected area electron diffraction pattern (inset) (b) HAADF-STEM image of $Sr_{1.8}Bi_{0.2}Nb_3O_{10}$ nanosheet

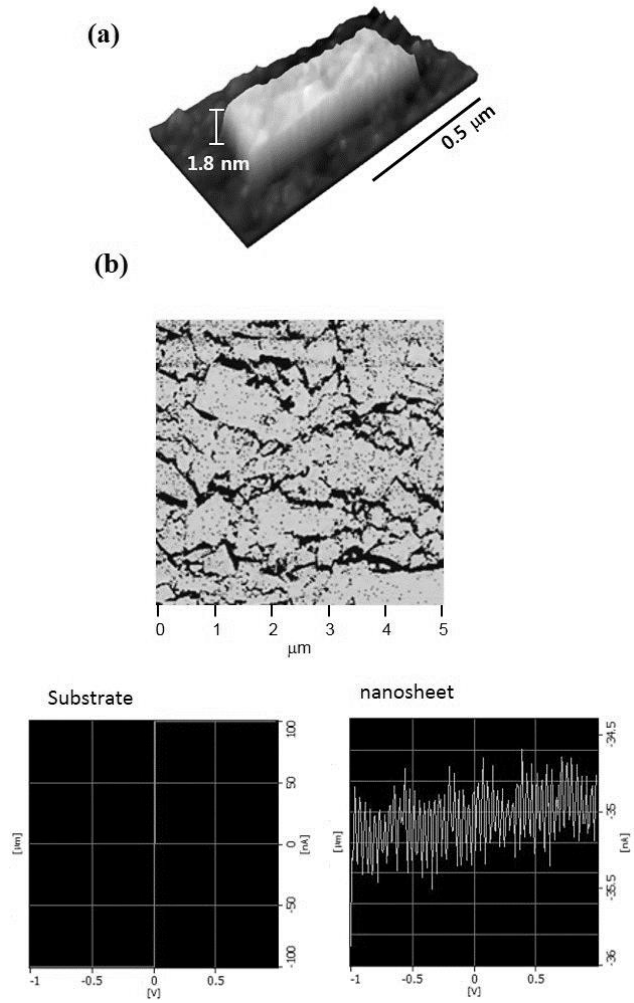

Figure 3.11. AFM and C-AFM images of $Sr_{1.8}Bi_{0.2}Nb_3O_{10}$ nanosheet

3.4. Conclusions

In this Chapter, we investigated the structural and dielectric properties of Dion-Jacobson phase $KSr_{2(1-x)}Bi_{2x}Nb_3O_{10}$ (x = 0, 0.1, 0.2, 0.3) layered perovskite ceramics. The dielectric permittivity increases from 31 to 348 while the dielectric loss decreases from 0.111 to 0.040 at 1 MHz as a consequence of substitution of Bi cations for Sr cations. To identify the origin of the enhanced dielectric constants, we employ Raman spectroscopy. As increasing the Bi substitution amount, the soft-mode vibration is decreased. The decreased hardening soft-mode vibration indicate the higher polarizability and leads larger dielectric permittivity. Likewise the structural and dielectric properties of $HSr_{2(1-x)}Bi_{2x}Nb_3O_{10}$ (x = 0, 0.1, 0.2, 0.3) ceramics were investigated, and the maximum dielectric permittivity was 814 with a dielectric loss of 0.027 in the formula of $HSr_{1.4}Bi_{0.6}Nb_3O_{10}$. Moreover, the $Sr_{2(1-x)}Bi_{2x}Nb_3O_{10}$ (x = 0, 0.1, 0.2, 0.3) colloidal nanosheets were successfully synthesized through 2-step cation exchanging process.

3.5. References

[1] M. Osada, K. Akatsuka, Y. Ebina, H. Funakubo, K. Ono, K. Takada and T. Sasaki, Acs Nano, 4, 5225 (2010).

[2] Z. Zhao, V. Buscaglia, M. Viviani, M. T. Buscaglia, L. Mitoseriu, A. Testino, M. Nygren, M. Johnsson and P. Nanni, Phys Rev B, 70 (2004).

[3] L. J. Sinnamon, M. M. Saad, R. M. Bowman and J. M. Gregg, Appl Phys Lett, 81, 703 (2002).

[4] Y. H. Kim, H. J. Kim, M. Osada, B. W. Li, Y. Ebina and T. Sasaki, Acs Appl Mater Inter, 6, 19510 (2014).

[5] M. Osada, K. Akatsuka, Y. Ebina, Y. Kotani, K. Ono, H. Funakubo, S. Ueda, K. Kobayashi, K. Takada and T. Sasaki, Jpn J Appl Phys, 47, 7556 (2008).

[6] M. Osada, Y. Ebina, H. Funakubo, S. Yokoyama, T. Kiguchi, K. Takada and T. Sasaki, Adv Mater, 18, 1023 (2006).

[7] W. Sugimoto, O. Terabayashi, Y. Murakami and Y. Takasu, J Mater Chem, 12, 3814 (2002).

[8] M. Osada and T. Sasaki, Adv Mater, 24, 210 (2012).

[9] M. Osada, S. Yoguchi, M. Itose, B. W. Li, Y. Ebina, K. Fukuda, Y. Kotani, K. Ono, S. Ueda and T. Sasaki, Nanoscale, 6, 14227 (2014).

[10] S. H. Kweon, M. Im, G. Han, J. S. Kim, S. Nahm, J. W. Choi and S. J. Hwang, J Eur Ceram Soc, 33, 907 (2013).

[11] Z. H. Zhong, W. P. Ding, Y. Chen, X. Y. Chen, Y. Y. Zhu and N. B. Min, Appl Phys Lett, 75, 1958 (1999).

[12] K. Saruwatari, H. Sato, T. Idei, J. Kameda, A. Yamagishi, A. Takagaki and K. Domen, J Phys Chem B, 109, 12410 (2005).

[13] K. S. Rao, P. M. Krishna, D. M. Prasad and D. Gangadharudu, J Mater Sci, 42, 4801 (2007).

[14] B. W. Li, M. Osada, Y. Ebina, T. C. Ozawa, R. Z. Ma and T. Sasaki, Appl Phys

Lett, 96 (2010).

[15] H. S. Gu, J. M. Xue, X. S. Gao and J. Wang, Mater Chem Phys, 75, 105 (2002).

[16] S. J. Penn, N. M. Alford, A. Templeton, X. R. Wang, M. S. Xu, M. Reece and K. Schrapel, J Am Ceram Soc, 80, 1885 (1997).

[17] S. George and M. T. Sebastian, J Am Ceram Soc, 93, 2164 (2010).

[18] H. Yim, S. Y. Yoo, Y. E. Sung and J. W. Choi, J Alloy Compd, 622, 373 (2015).

[19] C. S. Sun, P. Peng, L. R. Zhu, W. J. Zheng and Y. N. Zhao, Eur J Inorg Chem, 3864 (2008).

Chapter 4. Synthesis and characterization of Ag-substituted $Sr_2Nb_3O_{10}$ nanosheets

4.1. Introduction

In chapter 3, we have descripted the infortance of the developing Bi-substituted $Sr_2Nb_3O_{10}$ nanosheets. Likewise, we synthesis Ag-substituted $Sr_2Nb_3O_{10}$ nanoshets to confirm the effect of different A-site substitution. The structural and dielectric properties of layered perovskite $KSr_{2(1-x)}Ag_{2x}Nb_3O_{10}$ (x = 0, 0.1, 0.2, 0.3, 0.5, 0.7, 1.0) were investigated.

Dion-Jacobson (DJ) phases layered perovskite materials such as $LaNb_2O_7$ and $KCa_2Nb_3O_{10}$ have been widely investigated due to its great chemical activity including photocatalytic activity, ferroelectricity, dielectric and piezoelectricity[1-6]. Also, these layered materials consist of negatively charged perovskite slabs and occupied cations in the interlayer space, so these materials have weak bonding between each perovskite layers[7]. Therefore, the intercalated cation can be easily changed, so a various single crystal nanosheet can be simply delaminated into their elemental layers by exfoliating the layered structure precursors. Because of this fabulous characteristic, using two dimensional dielectric nanosheet have received enormous attention as a new direction to fabricate nano-scaled dielectric thin film because it is easy to obtain single crystal nanosheet by exchanging cation with simple chemical exfoliation process[8,9].

As a result, the post annealing process is not required and the dielectric properties are invariant depending on the thickness. The new concept of dielectric nanosheet thin film for MLCCs have attracted attention due to satisfaction of minimize

packaging size, having high capacitance, and absence of firing step in fabrication process. For these reasons, several exfoliated niobate materials such as $Ca_2Nb_3O_{10}$, $Sr_2Nb_3O_{10}$, and $Cs_4W_{11}O_{36}$ have been extensively reported.

Osada et al. reported the dielectric properties of $Ca_2Nb_3O_{10}$ and thin film which consist of NbO_6 octahedral units and show the dielectric permittivity over $\varepsilon_r = 200$[10]. Also, the mother materials were reported, and the dielectric response were changed from $\varepsilon_r = 300$ to 500 as controlling the number of NbO_6 octahedral units in $KCa_2Na_{m-3}Nb_mO_{3m+1}$ from m = 3 to 6. Likewise, the dielectric response of thin films from these starting materials show same tendency. These results intend that mother materials should have high dielectric response to obtain the high dielectric permittivity thin films. Therefore, here we synthesize new dielectric nanosheet materials in formula of $Sr_{2(1-x)}Ag_{2x}Nb_3O_{10}$, and we focus on not only dielectric nanosheet for thin film but also its starting materials as a microwave dielectric bulk ceramics.

4.2. Experimental section

4.2.1. Synthesis of $KSr_{2(1-x)}Ag_{2x}Nb_3O_{10}$ ceramics

In order to investigate the effect of silver substitution on potassium strontium niobate ceramics, the layered perovskite $KSr_{2(1-x)}Ag_{2x}Nb_3O_{10}$ (x = 0, 0.1, 0.2, 0.3, 0.5, 0.7, 1.0) (abbreviated as KSAN 0, KSAN 0.1 KSAN 0.2, KSAN 0.3, KASN 0.5, KASN 0.7, and KASN 1.0, respectively) were prepared by solid-state reaction using K_2CO_3 (≥99%, Aldrich, USA), $SrCO_3$ (≥99.9%, High Purity Chemistry, Japan), $AgCO_3$ (≥99%, Aldrich, USA), and Nb_2O_5 (≥99.9%, Aldrich, USA) in stoichiometric proportions as raw materials. The starting powders were ball-milled in anhydrous ethyl alcohol for 24 hours and dried at 110 ^oC for 24 hours. After grinding the dried mixture, calcination was applied at temperature of 1200 ^oC for 10 hours in covered alumina crucibles in the air. Then, the synthesized layered perovskite $KSr_{2(1-x)}Ag_{2x}Nb_3O_{10}$ powders (5 g) were continuously stirred in 7 M HNO_3 solution (200 ml) for 5 days. During this process, the K^+ ions between $Sr_{2(1-x)}Ag_{2x}Nb_3O_{10}$ layers were exchanged to H^+ ions and modified to $HSr_{2(1-x)}Ag_{2x}Nb_3O_{10}$ (x = 0, 0.1) (abbreviated as HSAN 0 and HSAN 0.1, respectively) ceramics. All products were washed by DI water several times to neutralize and dried at 60 ^oC for 24 hr. The synthesized KSAN and HSAN powders were compressed into compact disc shaped pellets of 12 mm in diameter with polyvinyl alcohol (PVA) binder under a pressure of 100 kgf/cm^2, and these pellets were carefully polished to form disk with 1 mm thickness. And then, the polished pellets were sintered at 1250 ^oC for 2 hours in a furnace and painted by a silver electrode on both sides. Then, the pellets were fired at 600 ^oC for 10 min in order to have good electrical contact for the estimation of dielectric properties.

4.2.2. Structural and dielectric properties measurements

The phase identification was carried out by X-ray diffraction (D/MAX-2500,

Rigaku, Japan) studies using Cu Kα radiation, and the micro structure was determined using scanning electron microscopy (Inspect F50, FEI, USA) while the chemical compositions of ceramics were characterized by energy dispersive X-ray spectroscopy. Fourier transform infrared spectroscopy (Nicolet iS 10, Thermo fisher scientific, USA) was carried out to obtain information of niobate bonding, and the spectra were measured from 500 to 1000 cm^{-1} at room temperature. Phase analysis was carried out with RAMAN spectra (inVia confocal Raman microscope, Renishaw plc, UK) from 100 to 800 cm^{-1} and near edge X-ray absorption fine structure (10D XAS KIST B/L, PAL, Korea). Dielectric measurements were taken using an impedance analyzer (Agilent Technologies HP 4294A, Santa Clara, USA) in the frequency range of 1 KHz to 1 MHz at room temperature.

4.2.3. Synthesis of $Sr_{1.8}Ag_{0.2}Nb_3O_{10}$ nanosheets

$Sr_{2(1-x)}Ag_{2x}Nb_3O_{10}$ (SAN) nanosheet were achieved from HABN powders by exfoliation in tetrabuthylammonium hydroxide (TBAOH) solution with a molar ration of $TBA^+ : H^+ = 1 : 1$. The 1 g HSAN powder is shaken in 200 ml TBAOH solution for 7 days, and the mixture is centrifuged at 15000 rpm for 20 min. The insertion of large size TBA^+ cations expands the each perovskite layers and exfoliates single nanosheets. The complete exfoliated nanosheet was confirmed by Transmission electron microscope (TEM) images and a selected area electron diffraction (SAED) pattern (Titan 80-300, FEI, USA) from the specimen that was prepared by dropping the diluted colloidal nanosheets on Cu grid. Also, the value of the zeta potential and near edge X-ray absorption fine structure was obtained.

4.3. Results and discussion

4.3.1. Syntheses and characterization of $KSr_{2(1-x)}Ag_{2x}Nb_3O_{10}$ ceramics.

The XRD patterns of KSAN ceramics are shown in Fig. 4.1. As mentioned in experimental section, the calcination and sintering temperature were reduced as increasing Ag substitution amount because Ag content decreased the melting temperature. According to XRD analysis, it is clearly seen that the peaks of KSAN 0 and 0.1 were indexed as a single phase with the literature values. However, the patterns of KSAN for x > 0.2 samples indicate that the main peak of DJ phases layered perovskite structure decrease with the adding Ag content, as presented by the cubic perovskite phase.

Fig. 4.2 shows the SEM micrographs of sintered surface of KSAN ceramics. The grain shapes of KSAN 0 seem to mostly plate shape, but the plate shape particles were disappeared and showed rod-like shape as adding Ag component. The two types of grains in the ceramics were observed in all samples above 0.2: one is the large plate shape grains and the other is the rod like small grain. Especially, the KSAN 0.7 shows very dense ceramics surface because of its better sinterability by Ag addition, and the plate shape particles were disappeared as increasing Ag component and showed rod-like shape which supposed from different phase. Therefore, we synthesis dielectric nanosheets with x=0.1 starting material only. Although nanosheets have been synthesized from only KSAN 0.1 materials, the dielectric properties of synthesized KSAN materials in other ranges are anlazied because that can be used as microwave dielectric bulk materials.

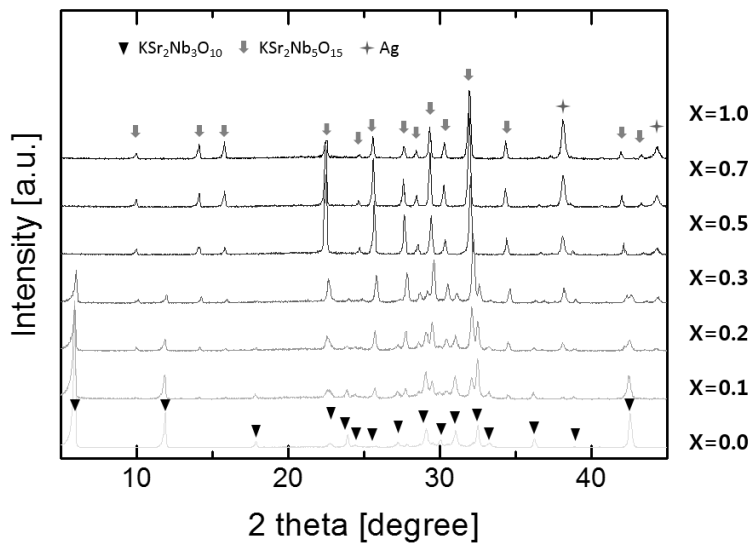

Figure 4.1. X-ray diffraction spectra of $KSr_{2(1-x)}Ag_{2x}Nb_3O_{10}$ ceramics.

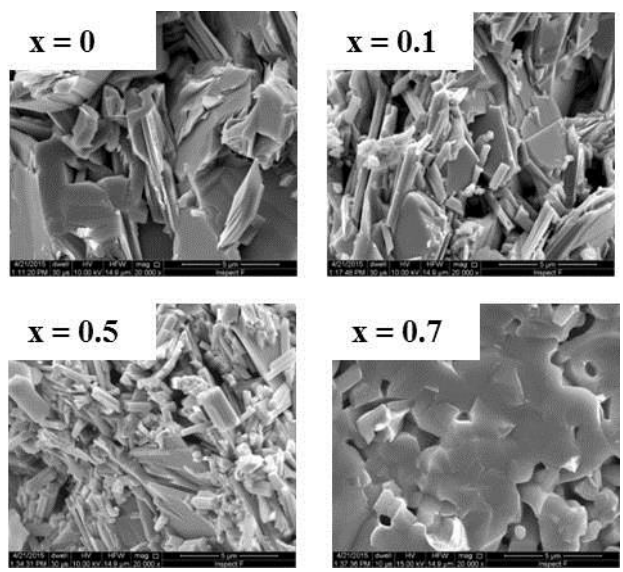

Figure 4.2. SEM images of $KSr_{2(1-x)}Ag_{2x}Nb_3O_{10}$ ceramics

4.3.2. Dielectric characterization of $KSr_{2(1-x)}Ag_{2x}Nb_3O_{10}$ ceramics.

The Fig.4.3 shows the Ag substitute amount dependence of the dielectric constant (ε_r) and dielectric loss (tan δ) at frequencies of 1 kHz and 1 MHz. The dielectric properties are greatly changed as substituting Ag compound, and this might be attributed to the appearance of the two different crystalline phases in one sintered body. Though sintering temperature is different, the dielectric permittivity of ceramics gradually increased with increasing Ag content until reached to KSAN 0.5.

The increased dielectric properties are analyzed by RAMAN measurement. The Raman spectra of KSAN samples are presented in Fig. 4.4. The observed peaks in 200 to 800 cm^{-1} are given information of niobate bonding, and the spectrum of KSAN 0 shows the major bands at 210, 250, 310, 540, and 750 cm^{-1} that is typical Raman spectrum[11,12] of the $KSr_2Nb_3O_{10}$. The absorptions around 310, 540, and 750 cm^{-2} mode are associated with the ν_5 (F_{2g}) bending mode, ν_2 (E_g) symmetry mode, and ν_1 (A_{1g}) symmetry of Nb-O bonding, respectively.

According to the silver substitution amount corresponds to smaller shift of peaks in low-frequency mode and thus it indicate the hardening soft-mode vibration are decreased as a result of enhancing. The balance between the ionic bonding and covalent bonding in the BO_6 octahedra generally determine the polarizability of perovskite material, and the lowest-frequency mode is connected to the coordinated dipole interactions of the perovskite layer. From the Raman spectra, the decreased hardening soft-mode vibration was observed and it leads to higher polarizabiltiy which make larger dielectric permittivity[13,14].

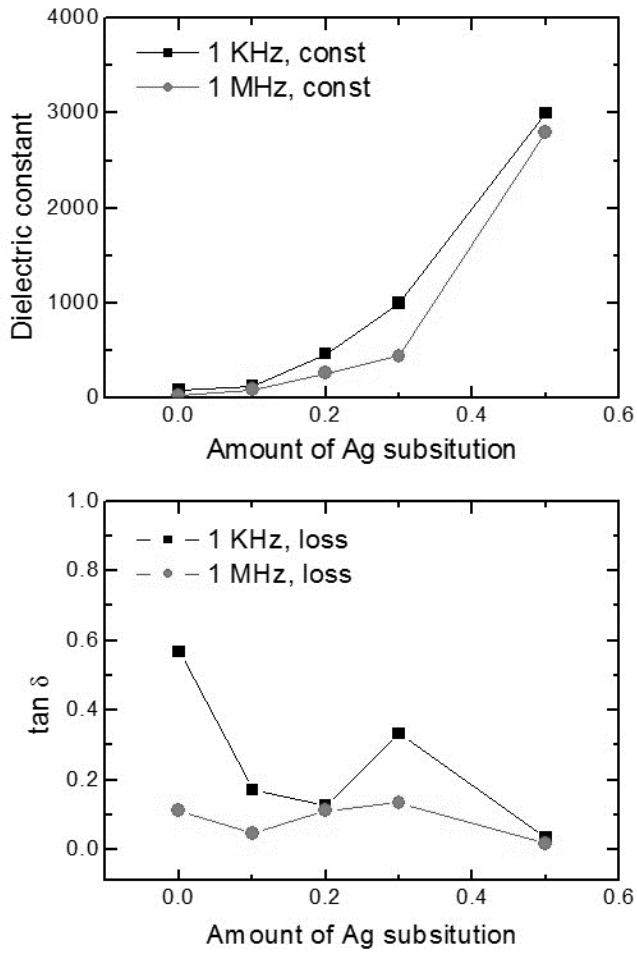

Figure 4.3. Dielectric properties of Properties of $KSr_{2(1-x)}Ag_{2x}Nb_3O_{10}$ bulk ceramics according to frequency. Each sample was pelletized with radius of 10 mm and thickness of 1 mm.

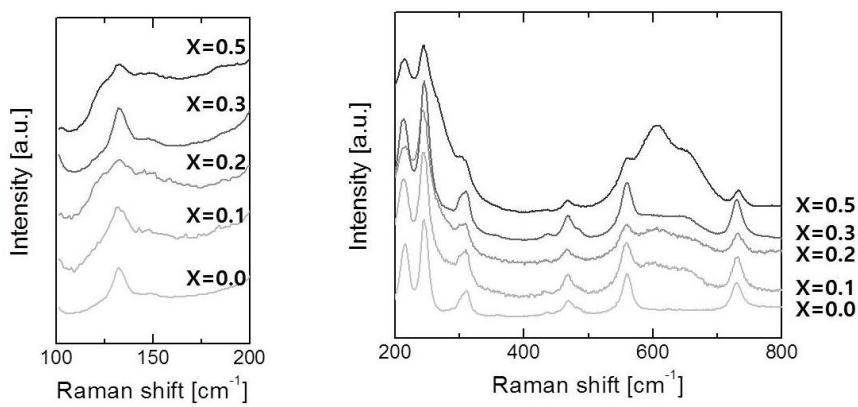

Figure 4.4. RAMAN measurement of $KSr_{2(1-x)}Ag_{2x}Nb_3O_{10}$ bulk ceramics.

4.3.3. Synthesis of $HSr_{2(1-x)}Ag_{2x}Nb_3O_{10}$ ceramics

As mentioned in 4.3.1 part, the KSAN for x > 0.2 samples indicate that the main peak of DJ phases layered perovskite structure decrease, as presented by the cubic perovskite phase. Therefore, we synthesis dielectric nanosheets with KSAN 0.1 ceramic.

In order to fabricate proton exchanged HSAN, the intercalated K^+ ions in the perovskite layers were exchanged to H^+ ions in HNO_3 solution. HSAN 0 and 0.1 are also well-indexed with the literature values, and the main peak of (002) is slightly shifted to lower angle (Fig. 4.5 (a)). The main reason is considered that the reaction with H^+ ions in DI water forms the H_3O^+ ions and this ions, which has larger ionic diameter than K^+ ions, mostly intercalated between each perovskite layers.

The absorption bands in the FTIR spectra of HSAN ceramics are presented in Fig. 4.5 (b). In FTIR spectrum of KSAN 0, there are clear absorption peaks associated with the NbO_6 octahedron such as 550, 700, and 910 cm^{-1}; the absorption at 550 cm^{-1} is assigned to the asymmetric stretching vibration of Nb-O bonding in central octahedral NbO_6; the absorption at 700 cm^{-1} is assigned to the asymmetric stretching vibration of Nb-O bonding in terminal distorted octahedral NbO_6; and the absorption at 910 cm^{-1} is assigned to the terminal Nb-O vibration. All niobate bonding are well maintained after Ag substitution.

The morphological analysis of HSAN 0 and 0.1 powders were investigated by SEM in Fig 4.6 (a). The both samples clearly show a lamella structure that included perovskite layers formed by cations. The layered microcrystal structure was maintained even after cation exchange. The EDS patterns was investigated to check remain K^+ ions in Fig. 4.6 (b). The peak around 330 keV, which is indexed to the K^+ ions, is not appeared that indicates that K^+ ions are fully exchanged.

Figure 4.7 shows the frequency dependence of the dielectric properties for HSAN 0 and 0.1 ceramics at room temperature. The powders were compressed into disc

shaped pellets of 12 mm in diameter under a pressure of 100 kgf/cm^2, and these pellets were polished to form disk with 0.5–1 mm thickness. Dielectric constant at 1 kHz increases from 96.6 to 332 and dielectric loss at 1 kHz decreased 0.4 to 0.03 with Ag substitution amount increasing from 0 to 0.1, and this phenomenon is similar to our previous studies.

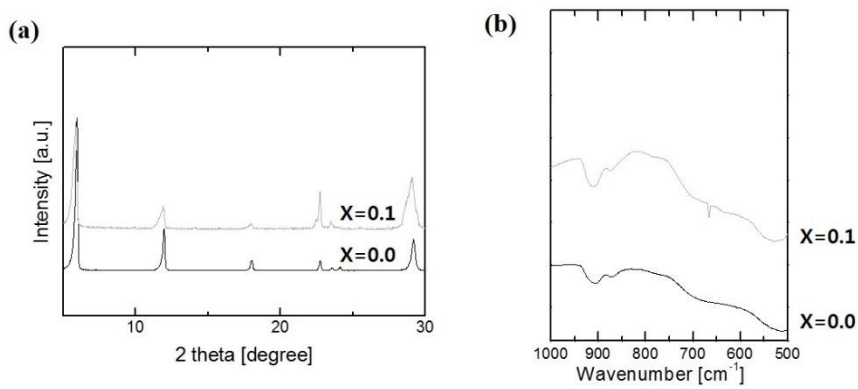

Figure 4.5. (a) XRD and (b) RAMAN measurement of $HSr_{2(1-x)}Ag_{2x}Nb_3O_{10}$ bulk ceramics.

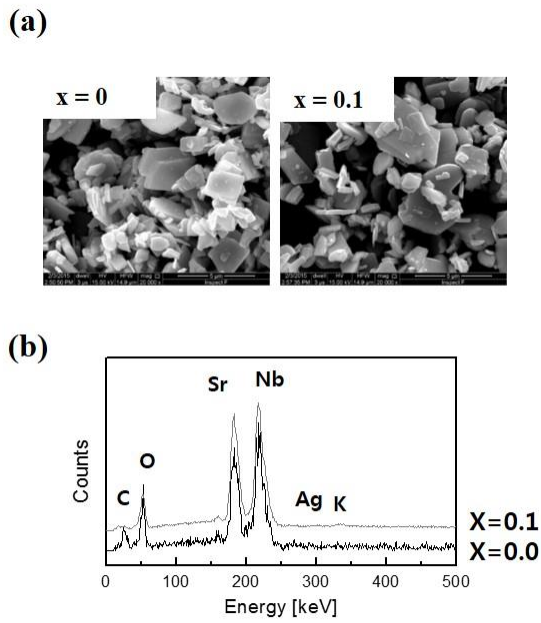

Figure 4.6. (a) SEM and (b) EDS measurement of $HSr_{2(1-x)}Ag_{2x}Nb_3O_{10}$ bulk ceramics.

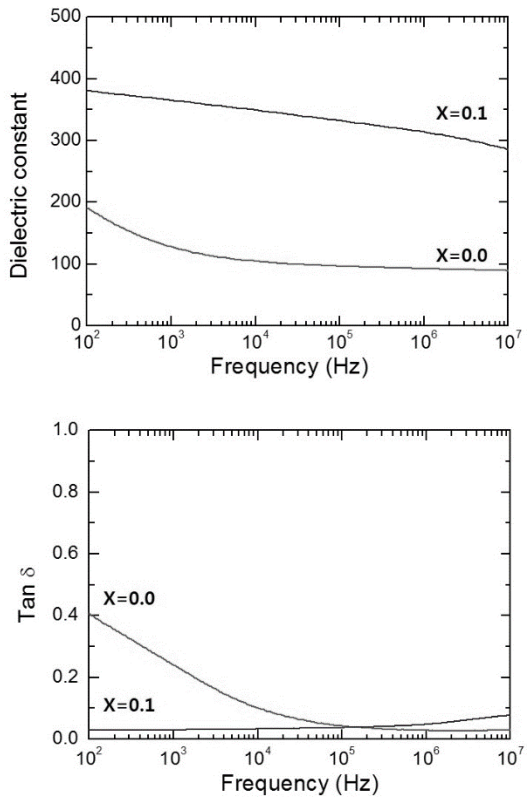

Figure 4.7. Dielectric properteis of $HSr_{2(1-x)}Ag_{2x}Nb_3O_{10}$ bulk ceramics.

4.3.4. Synthesis of $Sr_{1.8}Ag_{0.2}Nb_3O_{10}$ nanosheets.

After investigating the structural and dielectric properties of bulk materials, the negatively charged $Sr_{1.8}Ag_{0.2}Nb_3O_{10}$ (SAN 0.1) nanosheets are obtained by exfoliation of layered perovskite structure HSAN ceramics in TBAOH solution and surrounded by the positively charge TBA ions.

The TEM images and EDS mapping images of the delaminated SAN 0.1 nanosheets are shown in Fig. 4.8. The the lateral size of the nanosheets are about few micrometers. Compare with a nanosheet sample without Ag substitution, there were several spots in high contrast on the SAN 0.1 nanosheets. The agglomerate particles spots had an average size of 5 nm and indicate Ag nanoocrystals can be directly onto the perovskite nanosheets. The thickness of SAN 0.1 nanosheets are confirmed with AFM images. Fig. 4.9 shows typical AFM image of SAN 0.1 single layer nanosheet. The thickness of SBNO 0.1 nanosheets is 1.9 nm that is presumably due to the effect of Ag ions having a large ionic radius.

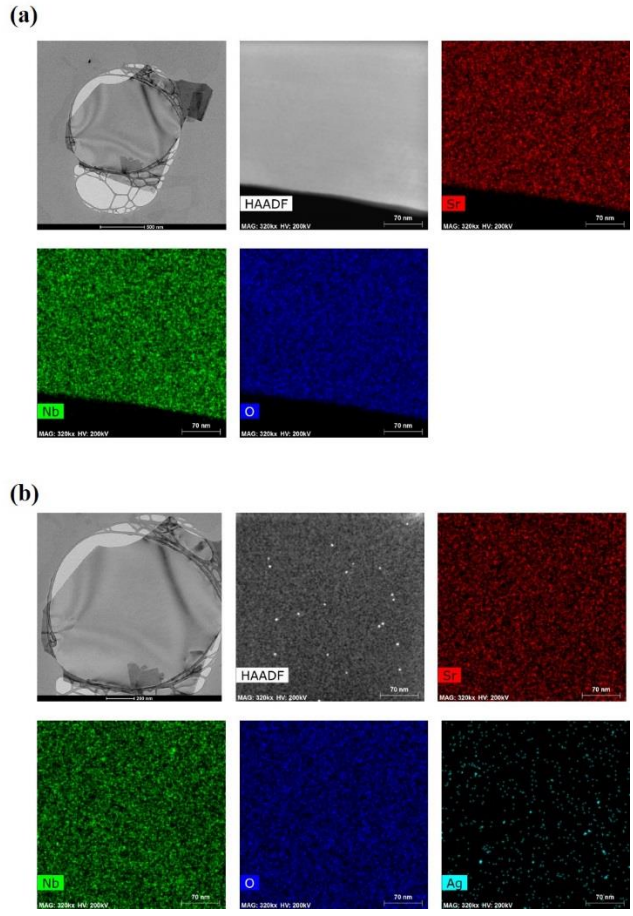

Figure 4.8. (a) TEM and EDS mappling images of $Sr_2Nb_3O_{10}$ nanosheets (b) TEM and EDS mappling images of $Sr_{1.8}Ag_{0.2}Nb_3O_{10}$ nanosheets.

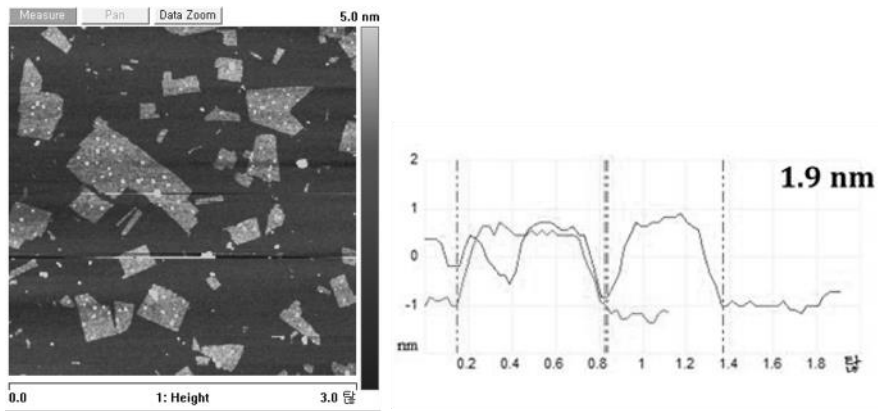

Figure 4.9. AFM images of $Sr_{1.8}Ag_{0.2}Nb_3O_{10}$ nanosheet

4.4. Conclusions

In this Chapter, we investigated the structural and dielectric properties of Dion-Jacobson phase $KSr_{2(1-x)}Ag_{2x}Nb_3O_{10}$ (x = 0, 0.1, 0.2, 0.3, 0.5, 0.7, 1.0) layered perovskite ceramics. However, there are the cubic perovskite phase with Ag metal phase except x = 0.1 sample, so we synthesis dielectric nanosheets with x = 0.1 starting material only. $HSr_{1.8}Ag_{0.2}Nb_3O_{10}$ ceramic, which is medium materials for exfoliation, were well obtained and showed enhanced dielectric permittivity from 96.6 to 332 with dielectric loss from 0.4 to 0.03 by Ag substitution. Moreover, the $Sr_{1.8}Ag_{0.2}Nb_3O_{10}$ colloidal nanosheets were successfully synthesized through TBA cation exchanging process.

4.5. References

[1] S. H. Kweon, M. Im, W. H. Lee, S. Nahm, J. W. Choi and S. J. Hwang, J Mater Chem C, 4, 178 (2016).

[2] Y. Tsujimoto, A. Kitada, M. Nishi, Y. Narumi, K. Kindo, T. Goko, Y. J. Uemura, A. A. Aczel, T. J. Williams, G. M. Luke, Y. Ajiro and H. Kageyama, J Phys Soc Jpn, 83 (2014).

[3] Y. Ebina, A. Tanaka, J. N. Kondo and K. Domen, Chem Mater, 8, 2534 (1996).

[4] M. Onoda, Z. P. Liu, Y. Ebina, K. Takada and T. Sasaki, J Phys Chem C, 115, 8555 (2011).

[5] L. Viciu, N. Liziard, V. Golub, T. A. Kodenkandath and J. B. Wiley, Mater Res Bull, 42, 196 (2007).

[6] B. W. Li, M. Osada, Y. Ebina, T. C. Ozawa, R. Z. Ma and T. Sasaki, Appl Phys Lett, 96 (2010).

[7] M. J. Geselbracht, H. K. White, J. M. Blaine, M. J. Diaz, J. L. Hubbs, N. Adelstein and J. A. Kurzman, Mater Res Bull, 46, 398 (2011).

[8] Y. S. Lee, H. Yim, S. Y. Yoo, B. K. Ju and J. W. Choi, J Alloy Compd, 711, 51 (2017).

[9] M. S. Khan, M. Osada, H. J. Kim, Y. Ebina, W. Sugimoto and T. Sasaki, Jpn J Appl Phys, 56 (2017).

[10] M. Osada, K. Akatsuka, Y. Ebina, H. Funakubo, K. Ono, K. Takada and T. Sasaki, Acs Nano, 4, 5225 (2010).

[11] Z. H. Zhong, W. P. Ding, W. H. Hou and Y. Chen, Chem Mater, 13, 538 (2001).

[12] G. Yang, W. H. Hou, X. M. Feng, L. Xu, Y. G. Liu, G. Wang and W. P. Ding, Adv Funct Mater, 17, 401 (2007).

[13] Y. Luspin, J. L. Servoin and F. Gervais, J Phys C Solid State, 13, 3761 (1980).

[14] P. S. Dobal, A. Dixit, R. S. Katiyar, Z. Yu, R. Guo and A. S. Bhalla, J Appl Phys, 89, 8085 (2001).

Chapter 5. Characterication of $Sr_{1.8}Bi_{0.2}Nb_3O_{10}$ nanosheets and its multilayer thin film

5.1. Introduction

In chapter 2-4, we investigated the developing various Dion-Jacosbon phase materials as substitution A-site of $Sr_2Nb_3O_{10}$ to enhance their dielectric properteis. Among them, the Bi-substituted $Sr_2Nb_3O_{10}$ nanosheets shows the most stable and excellent yield characteristics. Therefore, in this chapter, we invstigate the properties of multilayer thin films with $Sr_{1.8}Bi_{0.2}Nb_3O_{10}$ nanosheets. Moreover, we deposit thin films on transparent and flexible substrate to demonstrate the possivility of developiong transparent and flexible dielectric capacitors.

The search for high-k dielectric nanosheets materials, which store energy electrostatically, have been actively researched due to a versatile properties such as high dielectric permittivity and great thermal stability for advanced electronics[1-5]. In addition, the development of flexible and transparent electronics required the advanced dielectric materials[6-8].

Recently, various type of flexible dielectric materials based on polymer composite have been reported. However, thermal management is always required to enable the use of dielectric polymers in hightemperature applications[9]. 2-Dimensional (2D) Dion-Jacobson phase nanosheets have been shown high-k dielectric permittivity properties, which are undisturbed for the thickness and really stable in high-temperature about 500 ^oC, even for thickness down to 20 nm[10-13]. Moreover, these nanosheets are transparent and don't require to do a post annealing process, so 2D nanosheets can be deposited on flexible substrate.

Here, we atomically engineer the dielectric properties of $Sr_2Nb_3O_{10}$ by alloying their A-sites with high-valent Bi. This tilts the niobate octahedra and enhances the dielectric properties. We also investigate how doping the A-sites affect the symmetry, overall electronic charge, and dielectric properties of the material. The Bi-substituted $Sr_2Nb_3O_{10}$ thin films are demonstrated on flexible transparent conducting oxides as transparent and flexible dielectric capacitors.

5.2. Experimental section

5.2.1. Deposition nanosheets thin films by Langmuir-blodgett method

The $Sr_{1.8}Bi_{0.2}Nb_3O_{10}$ nanosheet solution were spread out on distilled water, and the transfer pressure was selected to 7 mN m^{-1} according to the π–A isotherm graph. Before transferred monolayer onto an Nb-doped $SrTiO_3$ substrate, UV-light irradiation in ozone was treated for the purpose of cleaning and making a hydrophilic surface. Highly close-packed monolayer thin film was transferred from the air/water interface to the Nb-doped $SrTiO_3$ substrate by pulling the substrate with the barrier compression. 10 layer SBNO thin film was transferred by multiple transfer through the same procedure. Then, multilayer thin film was irradiated with UV-light for 24 hrs to decompose the residual organic species.

5.2.2. Structural and dielectric properties measurements

The film quality was characterized by HRTEM and AFM. Cross-sectional HRTEM was carried out using a Hitachi H-9000 microscope operating at 200 kV with a point resolution of 0.1 nm. The surface morphology was analyzed using an SII Nanotechnology E-Sweep AFM.

In order to measure the electrical properties, 30 nm thickness Au top-electrodes were deposited by the E-beam evaporator. The dielectric properties and leakage properties were measured with an impedance analyzer (Agilent 4294A precision, Santa Clara, USA) and a semiconductor parameter analyzer (Keithley 4200 SCS, Ohio, USA). The EXAFS spectra of nanosheets were measured at 10C beamline at Pohang Accelerator Laboratory, Pohang, Korea. Higher harmonics were effectively removed by detuning of the incident beam to 60% of maximum intensity. Three ionization chambers filled with He and N_2-gas were used to record the intensity of the incident and the transmitted X-rays. The sample is placed between the first and second ionization chamber, while SrO for energy calibration is placed between the

second and third ionization chamber. Under stationary conditions, extended X-ray absorption fine-structure (EXAFS) measurements were performed around the Sr *K*-edge in the step scanning mode.

5.3. Results and discussion

5.3.1. Characterization of $Sr_{1.8}Bi_{0.2}Nb_3O_{10}$ nanosheets

The $Sr_{1.8}Bi_{0.2}Nb_3O_{10}$ nanosheets are synthesized by chemical exfolation method as shown in in Chap. 3. In order to confirm the local structure of the nanosheets, EXAFS analysis was carried out. Fig. 5.1 shows the X-ray absorption near edge spectra for SBNO 0 and SBNO 0.1. Main edges of both the materials are 16,102 and 16,103 eV which reveals that the Sr valence states are approximately identical in both materials (Fig. 5.1 (a) and (b)). The first derivative spectra of these materials also confirm this. Fig. 5.1 (c) shows the χ(k) spectra of both materials. χ(k) oscillations of both materials are almost the same, suggesting that the coordination of both materials are almost same. Bi substitution does not affect the local atomic order of SBNO 0 material.

Fig. 5.2 shows the experimental and the simulated Fourier transform of the extended X-ray absorption fine structure (EXAFS) spectra of SBNO 0 and SBNO 0.1 nanosheets. For the simulation, Athena software was used to sum the data, identify the beginning of the absorption edge (E_0), fit pre-edge and post-edge backgrounds, and obtain the normalized absorbance χ as a function of the modulus of the photoelectron wave vector k[14].

The fitting was carried out using ARTEMIS in the k range 3–11 Å. The EXAFS data is Fourier transformed to R-space to investigate the atomic structure and relative bond-lengths with respective to the absorbing atoms[14,15]. The atomic structure for SBNO 0 and SBNO 0.1 nanosheets were generated using the ATOM and FEFF from the parameters described in reports of similar systems[,16,17]. Parameters obtained from the simulation are collated in Table 5.1. It is clear from the table that the structure of both materials remains almost the same after Bi substitution, however, the coordination number reduces after Bi substitution. One more thing is that Sr-Nb shell show shrinkage after Bi-substitution.

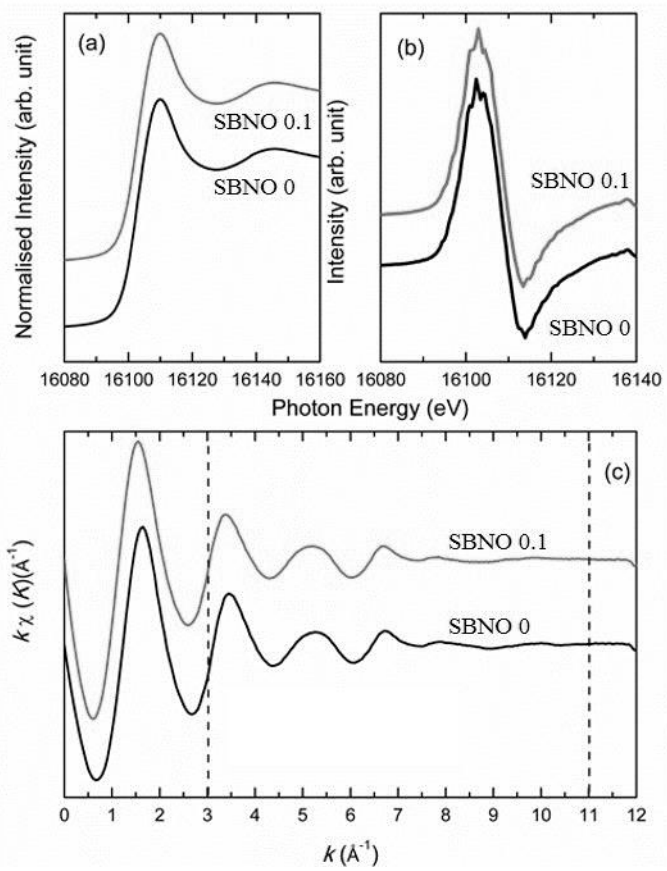

Figure 5.1. Sr *K*-edge (a) XANES (b) first derivative spectra and (c) $\chi(k)$ spectra of $Sr_2Nb_3O_{10}$ and $Sr_{1.8}Bi_{0.2}Nb_3O_{10}$ nanosheets.

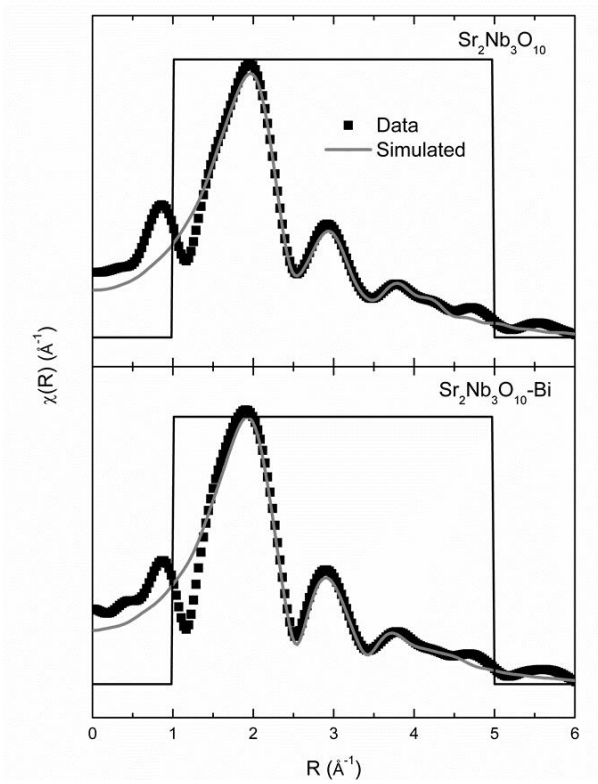

Figure 5.2. Fourier transform of Sr *K*-edge EXAFS spectra of $Sr_2Nb_3O_{10}$ and $Sr_{1.8}Bi_{0.2}Nb_3O_{10}$ nanosheets.

Shell	N	σ^2 (Å^2)	R (Å)	ε_o (eV)	R-factor/Happiness*
$Sr_2Nb_3O_{10}$					
Sr-O	8.5	0.018	2.60	3.3	0.046/75
Sr-O	4.2	0.016	2.96		
Sr-Nb	4.2	0.016	3.43		
Sr-Nb	4.2	0.012	3.63		
Sr-Sr	4.2	0.014	3.86		
Sr-O	8.5	0.023	4.54		
Bi doped $Sr_2Nb_3O_{10}$					
Sr-O	5.9	0.016	2.56	-1.94	0.07/54
Sr-O	3.0	0.016	2.95		
Sr-Nb	3.0	0.011	3.32		
Sr-Nb	3.0	0.010	3.49		
Sr-Sr	3.0	0.015	3.72		
Sr-Bi	1.4	0.028	3.73		
Sr-O	5.9	0.013	5.09		

Table 5.1. Co-ordination number (N), radial distance (R) and Debye-Waller factor (σ2) of $Sr_2Nb_3O_{10}$ and Bi doped $Sr_2Nb_3O_{10}$ materials

5.3.2. Characterization of $Sr_{1.8}Bi_{0.2}Nb_3O_{10}$ multilayer thin films

We fabricated SBNO 0.1 multilayer nanofilms using Langmuir-Blodgett (LB) method at room-temperature. As spreading the SBNO 0.1 colloidal nanosheet on the distill water surface and pressing the barrier, a monolayer film can be achieved at air/water interface. Pressure-Area (π-A) isotherm graph of SBNO 0.1 colloidal suspensions is presented in Fig. 5.3, and the surface pressure goes up without the addition of amphiphilic additives due to the moderate amphiphilic nature of TBA ions. The isotherm graph shows a suitable surface pressure of 10 mN m^{-1}. The highly close-packed monolayer film is transferred to the substrate during the lifting-up process. Highly uniform, atomically flat, and dense monolayer thin film is deposited by AFM images in Fig. 5.4 inset. The LB transfer process is repeated 10 times to get a 10 layer stacked multilayer thin film, and the deposition procedure is monitored through UV-Visible absorbance spectra. The multilayer stacking process is confirmed by a linear increment in spectra intensity in Fig. 5.4.

Fig. 5.5 shows the XRD pattern for the 10 layer deposited SBNO 0.1 thin film. All peak positions are indexed to perovskite niobate layer and assigned with basal reflections (00l) due to its parallel nature[18]. A cross-sectional HRTEM observation was carried out in Fig. 5.6 and it shows the flat and well-ordered lamellar structure in multilayer thin film, and each layer shows three parallel fringes because of the apex-sharing NbO_6 octahedra[19]. The total thickness of 10 layer-stacked SBNO 0.1 thin film is measured to be approximately 18 nm.

In order to fabricate a dead-layer-free perovskite nanosheet thin films, we deposited SBNO 0.1 nanosheets directly on the conductive Nb-doped $SrTiO_3$ which has similar lattice parameter with niobate nanosheets. Fig. 5.7 shows the dielectric properties and leakage current characteristics of Au/$Sr_{1.8}Bi_{0.2}Nb_3O_{10}$ (18 nm)/Nb-doped $SrTiO_3$. The Au top-electrode of capacitors was deposited by evaporation using a shadow mask with an aperture of 10 μm radius. The leakage current density was measured

by biasing the top-electrode of Au from 0 V to 2 V, and it exhibited very stable insulating properties (~ 10^{-7} A cm^{-2}) in all ranges. The dielectric properties of 18 nm dielectric thin film according to frequency was carried out. The dielectric permittivity exhibit a constant value of 540 with low dispersion (< 10 %) in the range from 1 kHz to 1 MHz, and the dielectric loss values was 0.01 to 0.05 in the range from 1 kHz to 1 MHz. The dielectric permittivity is 10 times larger than that of $(Ba_{1-x}Sr_x)TiO_3$ films and 2 times larger than $Sr_2Nb_3O_{10}$ nanosheets thin film with the same thickness. This enormous value is the effect of better polarizability of Bi ions and the low interfacial dead layer. The current fabrication process of MLCCs involves the incomplete screening that causes unclear interface between dielectric and electrode and firing step that causes defect and strains in the dielectric layer. Whereas there is no need to do post-annealing in case of the perovskite nanosheets thin films, so there is no degradation of interface and thermal strain. Clearly, perovskite nanosheets afford high capacitances with molecularly thin thickness.

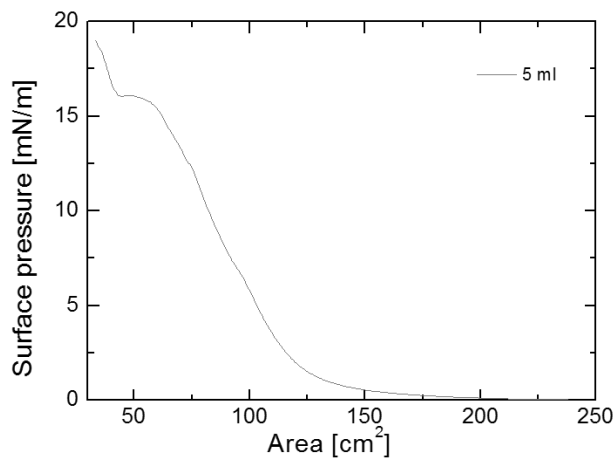

Figure 5.3. Isotherm graph of $Sr_{1.8}Bi_{0.2}Nb_3O_{10}$ nanosheets.

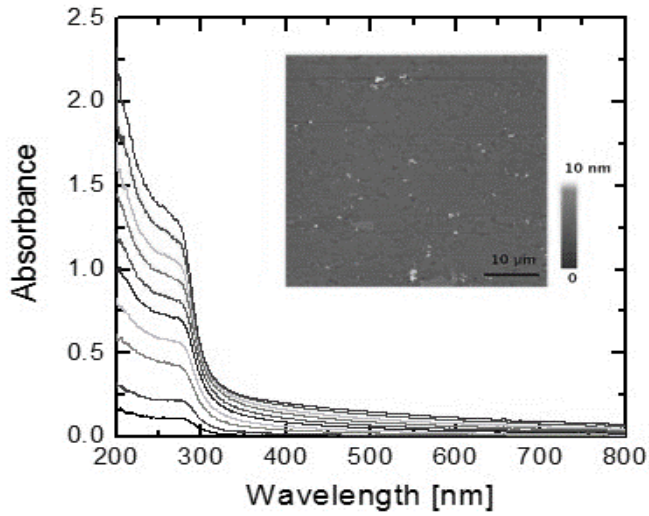

Figure 5.4. UV-visible absoption spectra for every single layer deposition of $Sr_{1.8}Bi_{0.2}Nb_3O_{10}$ on both sides of a quartz glass substrate.

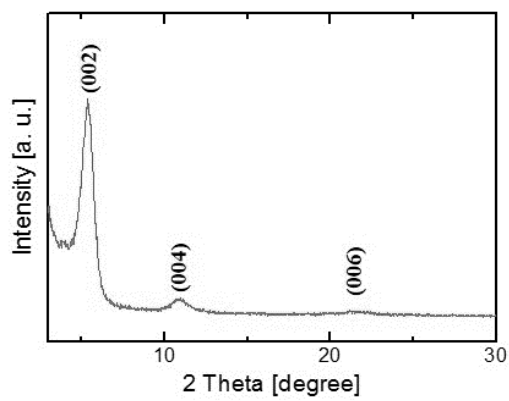

Figure 5.5. XRD pattern of 10 layer deposited $Sr_{1.8}Bi_{0.2}Nb_3O_{10}$ nanosheets thin film by Langmuir-Blodgett method**.**

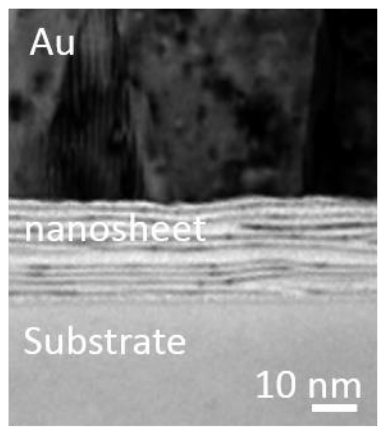

Figure 5.6. Cross-sectional TEM image of $Sr_{1.8}Bi_{0.2}Nb_3O_{10}$ nanosheets thin film.

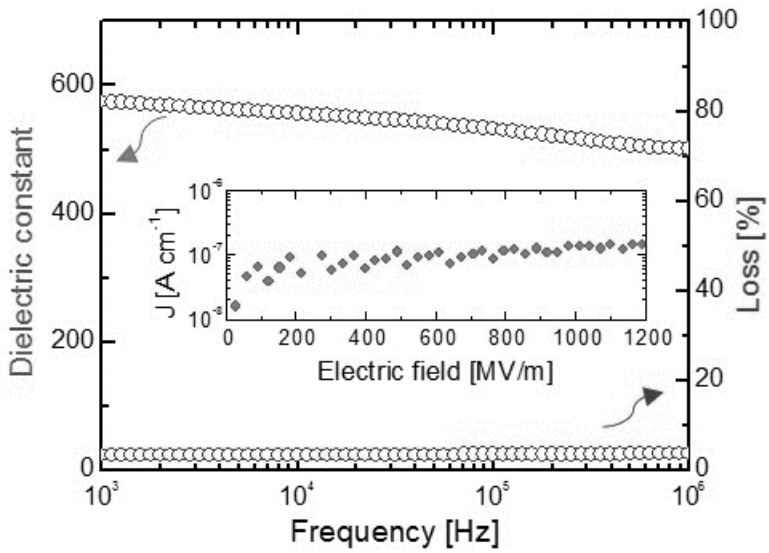

Figure 5.7. Frequency dependence of dielectric properties and leakage current density of thin film with 10 μm Au top electrode.

5.3.3. Fabrication transparent dielectric capacitor

In addition, the deposition of a thin film on flexible polymer substrates is possible because the fabrication process of this SBNO 0.1 film doesn't require the thermal treatment process. Therefore, we deposited SBNO 0.1 film on PET substrate with Zn (2.43 wt%)-doped SnO_2 oxide/metal/Zn (2.43 wt%)-doped SnO_2 oxide (OMO) multilayered transparent conducting electrode to realize the transparent dielectric capacitors. The OMO multilayer, which has the total thickness of 72 nm with resistivity of about 5.33×10^{-5} Ω cm and the transmittance > 85 % at 550 nm[20], was deposited by the on-axis RF sputtering (oxide layer) and DC sputtering (Ag layer).

A typical UV-VIS spectrum of $(SBNO\ 0.1)_{10}$ film with a thickness of 18 nm is shown in Fig. 5.8 (a). It shows a transmission of 95% without substrates, and the transmittance including PET substrate is 82.1 % as shown in Fig. 5.8 (b). The OMO were deposited as the top and bottom electrodes to realize transparent dielectric capacitor. The capacitor, which consists of OMO top electrode/ $(SBNO\ 0.1)_{10}$ /OMO bottom electrode structure, shows high transparency of 74.4 % at the 550 nm wavelength.

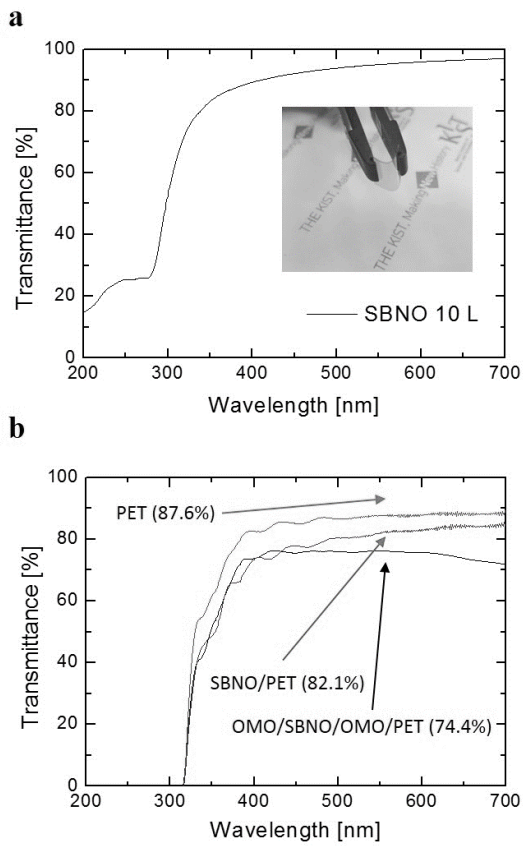

Figure 5.8. (a) Optical transmittance of a 10 layer deposited $Sr_{1.8}Bi_{0.2}Nb_3O_{10}$ thin film on PET substrate. Inset photograph shows a folded thin film. (b**)** Optical transmittance of PET substrate, $(Sr_{1.8}Bi_{0.2}Nb_3O_{10})_{10}$ thin film on PET substrate, and OMO(Zn-doped SnO_2 oxide/metal/oxide) top electrode/ $(Sr_{1.8}Bi_{0.2}Nb_3O_{10})_{10}$ /OMO bottom electrode.

5.4. Conclusions

In conclusion, we have successfully synthesized new composition dielectric nanosheets by cation exchange process and fabricated thin films by Langmuir-Blodgett method. The dielectric nanosheets thin film shows dielectric permittivity of 540 with low dielectric loss under 5 % and high transmission of 95%. Therefore, we believe that this material are desirable for various type of dielectric applications. Moreover, this transparent dielectrics may open the avenue to new and improved devices such as flexible and transparent devices far beyond the conventional top-down processes.

5.5. References

[1] J. S. Meena, M. C. Chu, R. Singh, H. P. D. Shieh, P. T. Liu and F. H. Ko, J Mater Sci-Mater El, 24, 1807 (2013).

[2] W. J. Sarjeant, I. W. Clelland and R. A. Price, P Ieee, 89, 846 (2001).

[3] H. Ogihara, C. A. Randall and S. Trolier-McKinstry, J Am Ceram Soc, 92, 1719 (2009).

[4] I. M. Reaney and D. Iddles, J Am Ceram Soc, 89, 2063 (2006).

[5] A. V. Shinde, S. A. Pande, S. S. Joshi and S. A. Acharya, Ferroelectrics, 502, 187 (2016).

[6] Y. Zhou, L. Wang, Y. H. Ma, D. Chen, C. W. Zhao and W. T. Yang, J Appl Polym Sci, 132 (2015).

[7] W. Yang, K. Song, Y. Jung, S. Jeong and J. Moon, J Mater Chem C, 1, 4275 (2013).

[8] Y. Yang, G. Chiesura, T. Vervust, F. Bossuyt, G. Luyckx, J. Degrieck and J. Vanfleteren, Sensor Actuat a-Phys, 243, 103 (2016).

[9] Q. Li, L. Chen, M. R. Gadinski, S. H. Zhang, G. Z. Zhang, H. Y. Li, A. Haque, L. Q. Chen, T. N. Jackson and Q. Wang, Nature, 523, 576 (2015).

[10] J. Kimura, I. Takuwa, M. Matsushima, T. Shimizu, H. Uchida, T. Kiguchi, T. Shiraishi, T. J. Konno, T. Shibata, M. Osada, T. Sasaki and H. Funakubo, Sci Rep-Uk, 6 (2016).

[11] Q. C. Jia, X. Y. Huang, G. Y. Wang, J. C. Diao and P. K. Jiang, J Phys Chem C, 120, 10206 (2016).

[12] B. W. Li, M. Osada, T. C. Ozawa, R. Ma, K. Akatsuka, Y. Ebina, H. Funakubo, S. Ueda, K. Kobayashi and T. Sasaki, Jpn J Appl Phys, 48 (2009).

[13] Y. H. Kim, M. Osada, L. Dong, H. J. Kim and T. Sasaki, J Ceram Soc Jpn, 123, 335 (2015).

[14] K. Okamoto, H. Sato, K. Saruwatari, K. Tamura, J. Kameda, T. Kogure, Y.

Umemura and A. Yamagishi, J Phys Chem C, 111, 12827 (2007).

[15] C. X. Wang, M. Osada, Y. Ebina, B. W. Li, K. Akatsuka, K. Fukuda, W. Sugimoto, R. Z. Ma and T. Sasaki, Acs Nano, 8, 2658 (2014).

[16] L. J. Sinnamon, M. M. Saad, R. M. Bowman and J. M. Gregg, Appl Phys Lett, 81, 703 (2002).

[17] M. Osada, Y. Ebina, H. Funakubo, S. Yokoyama, T. Kiguchi, K. Takada and T. Sasaki, Adv Mater, 18, 1023 (2006).

[18] M. Osada, K. Akatsuka, Y. Ebina, H. Funakubo, K. Ono, K. Takada and T. Sasaki, Acs Nano, 4, 5225 (2010).

[19] Z. Zhao, V. Buscaglia, M. Viviani, M. T. Buscaglia, L. Mitoseriu, A. Testino, M. Nygren, M. Johnsson and P. Nanni, Phys Rev B, 70 (2004).

[20] Y. Cho, N. S. Parmar, S. Nahm and J. W. Choi, J Alloy Compd, 694, 217 (2017).

국문초록

최근 초박막 유전체층을 이용한 적층형 세라믹 캐패시터, 고이동도 박막 트랜지스터를 위한 게이트 유전막 같은 차세대 전자 소자를 위한 고유전율 박막에 대한 요구가 크게 증가하고 있다. 가장 대표적으로 사용되는 유전체 박막은 $(Ba,Sr)TiO_3$ 조성의 페로브스카이트 박막이다. 이러한 유전체 박막의 경우 두께가 감소할수록 size-effect에 의하여 유전율이 감소하게 되는 단점이 있다. 또한 얇은 두께에서 박막의 신뢰성과 파괴강도를 증가시키기 어렵다는 한계점이 있다.

이러한 한계점을 극복할 수 있는 물질로 이차원 나노시트를 이용한 박막이 주목받고 있다. 특히 Dion-Jacobson 상의 유전체 재료는 고상의 세라믹 재료에서 뿐만 아니라 박리된 나노시트 형태에서도 우수한 특성을 나타내기 때문에 주목받고 있다. 예를들어, $Ca_2Nb_3O_{10}$ (유전율 = 200) 및 $Sr_2Nb_3O_{10}$ (유전율 = 240) 나노시트 박막은 우수한 유전율과 낮은 유전 손실값을 가지고 있다. 이러한 나노시트는 층상구조를 가지고 있는 모조성인 $K(Ca\ or\ Sr)_2Nb_3O_{10}$의 K^+ 이온을 H^+ 이온 및 TBA^+ 이온으로 치환하여 쉽게 얻을 수 있다. 페로브스카이트 구조를 가지는 $(Ca\ or\ Sr)_2Nb_3O_{10}$층에 큰 이온 반경을 가지는 TBA^+ 이온이 치환되면서 자연스럽게 페로브스카이트 층이 박리되게 된다. 따라서 모조성의 조성을 바꿈으로서 쉽게 새로운 조성의 나노시트를 합성할 수 있다. 또한 이차원 나노시트 박막은 열처리가 필요없어 다양한 기판에 적용될 수 있다.

하지만 현재까지 개발된 유전체 박막의 유전율은 $(Ba,Sr)TiO_3$ 조성의 페로브스카이트 박막보다 훨씬 낮은 값을 나타내며 단일 나노 시트의 전기적 특성에 관한 연구는 아직도 보고된 바가 없다. 따라서 우리는 페

로브스카이트 층의 A-site를 치환하여 우수한 유전 특성을 나타내는 새로운 조성의 Dion-Jacobson 물질을 합성하고 새로운 조성의 나노시트를 합성하고자 하였다.

1장에서 이차원 유전체 나노시트 박막에 대한 배경 및 이전 연구에 대한 간략한 설명을 마친 후, 2장에서 $Ca_2Nb_3O_{10}$ 및 $Sr_2Nb_3O_{10}$의 모조성인 $KCa_{2(1-x)}Sr_{2x}Nb_3O_{10}$ 조성의 구조적 특송과 유전 특성을 분석하였다. 나노시트에서와 마찬가지로 우수한 분극 특성을 갖는 Sr의 치환량이 증가할수록 벌크에서의 유전 특성도 증가하는 것을 확인할 수 있었다. 또한 $Ca_2Nb_3O_{10}$ 및 $Ca_{0.8}Sr_{1.2}Nb_3O_{10}$ 조성의 나노시트를 합성하여 전기영동법으로 박막의 특성을 비교하였고 벌크에서와 마찬가지로 Sr이 치환 된 나노시트의 박막특성이 더 우수한 것을 확인하였다.

다음 3, 4장에서는 $KSr_{2(1-x)}M_{2x}Nb_3O_{10}$ 조성을 가지는 유전 물질을 합성하였다. 3장에서는 A-site인 Sr을 분극 특성이 더 우수한 Bi로 치환하는 연구를 진행하였다. $KSr_{2(1-x)}Bi_{2x}Nb_3O_{10}$의 조성에서 Bi의 함량이 증가함에 따라 1 MHz에서 유전율은 31 에서 348으로 증가하고 유전 손실은 0.111 에서 0.040으로 감소하는 것을 확인하였다. 이는 우수한 분극 특성을 가지는 Bi 이온이 유전 분극을 향상시켰기 때문이며 RAMAN 및 DFT 분석을 통하여 확인되었다. 또한 $Sr_{2(1-x)}Bi_{2x}Nb_3O_{10}$ 조성의 나노시트를 성공적으로 합성하였다.

4장에서는 $KSr_{2(1-x)}M_{2x}Nb_3O_{10}$ 조성의 A-site인 Sr을 우수한 분극 특성을 가지는 Ag로 치환하였다. Ag의 함량이 증가할수록 유전 특성은 증가하였지만 x = 0.1 이상이 되는 경우 Ag가 금속으로 따로 존재하며 이차상 나타나는 것을 확인하였다. 따라서 나노시트는 x = 0.1 조성에서 합성되었고 AFM 및 TEM을 통하여 나노시트의 박리를 확인할 수 있었

다.

5장에서는 다양하게 합성 된 나노시트 조성 중 우수한 안정성 및 수득률을 가지는 $Sr_{1.8}Bi_{0.2}Nb_3O_{10}$ 나노시트에 대한 박막의 특성을 확인하였다. 박막은 랭뮤어-블로젯 증착법을 통하여 형성되었으며 10층을 증착하여 18 nm를 가지는 박막을 제작하였다. 이러한 나노시트는 Bi가 치환되기 전 보다 2배 이상의 우수한 유전율을 나타내는 것이 확인 되었다. 또한 나노시트 증착이 상온에서 이뤄지기 때문에 차세대 전자소자에 적용 가능성을 탐색하기 위하여 투명한 유연 기판에 캐패시터를 구현하여 추후 다양한 전자소자에 응용 될 수 있을 것으로 기대된다.

주요어: 랭뮤어-블로젯 증착, 유전체 나노시트, 유전체 캐패시터, A-site 치환, 스트론튬 나이오베이트

학번: 2014-31080